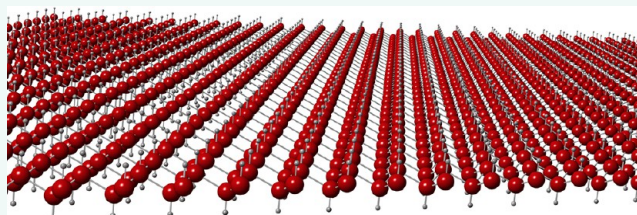


Progress, Challenges, and Opportunities in Two-Dimensional Materials Beyond Graphene

Sheneve Z. Butler,^{†,○} Shawna M. Hollen,^{‡,○} Linyou Cao,[§] Yi Cui,[⊥] Jay A. Gupta,[‡] Humberto R. Gutiérrez,[□] Tony F. Heinz,^{||} Seung Sae Hong,[⊥] Jiaxing Huang,[†] Ariel F. Ismach,[#] Ezekiel Johnston-Halperin,[‡] Masaru Kuno,[△] Vladimir V. Plashnitsa,[△] Richard D. Robinson,[▼] Rodney S. Ruoff,[#] Sayeef Salahuddin,[△] Jie Shan,[▽] Li Shi,[○] Michael G. Spencer,[●] Mauricio Terrones,[□] Wolfgang Windl,[■] and Joshua E. Goldberger^{†,*}

[†]Department of Chemistry and Biochemistry and [‡]Department of Physics, The Ohio State University, Columbus, Ohio 43210, United States, [§]Department of Materials Science and Engineering, North Carolina State University, Raleigh, North Carolina 27607, United States, [⊥]Department of Materials Science and Engineering, Stanford University, Palo Alto, California 94305, United States, ^{||}Department of Physics and Electrical Engineering, Columbia University, New York, New York 10027, United States, [†]Department of Materials Science and Engineering, Northwestern University, Evanston, Illinois 60208, United States, [#]Department of Mechanical Engineering and the Materials Science and Engineering Program, The University of Texas at Austin, Austin, Texas 78712, United States, [△]Department of Chemistry and Biochemistry, University of Notre Dame, Notre Dame, Indiana 46556, United States, [▼]Department of Materials Science and Engineering, Cornell University, Ithaca, New York 14853, United States, [△]Department of Electrical Engineering and Computer Sciences, University of California, Berkeley, California 94720, United States, [▽]Department of Physics, Case Western Reserve University, Cleveland, Ohio 44106, United States, [○]Department of Mechanical Engineering, The University of Texas at Austin, Austin, Texas 78712, United States, [●]Department of Electrical and Computer Engineering, Cornell University, Ithaca, New York 14850, United States, [□]Department of Physics, The Pennsylvania State University, University Park, Pennsylvania 16802, United States, and [■]Department of Materials Science and Engineering, The Ohio State University, Columbus, Ohio 43210, United States. [○]These authors contributed equally.

ABSTRACT Graphene's success has shown that it is possible to create stable, single and few-atom-thick layers of van der Waals materials, and also that these materials can exhibit fascinating and technologically useful properties. Here we review the state-of-the-art of 2D materials beyond graphene. Initially, we will outline the different chemical classes of 2D materials and discuss the various strategies to prepare single-layer, few-layer, and multilayer assem-



bly materials in solution, on substrates, and on the wafer scale. Additionally, we present an experimental guide for identifying and characterizing single-layer-thick materials, as well as outlining emerging techniques that yield both local and global information. We describe the differences that occur in the electronic structure between the bulk and the single layer and discuss various methods of tuning their electronic properties by manipulating the surface. Finally, we highlight the properties and advantages of single-, few-, and many-layer 2D materials in field-effect transistors, spin- and valley-tronics, thermoelectrics, and topological insulators, among many other applications.

KEYWORDS: two-dimensional materials · graphene · nanosheets · graphane · van der Waals epitaxy · van der Waals solid

Two-dimensional (2D) materials have historically been one of the most extensively studied classes of materials due to the wealth of unusual physical phenomena that occur when charge and heat transport is confined to a plane. Many materials with properties dominated by their two-dimensional structural units such as the layered metal dichalcogenides (LMDCs), copper oxides, and iron pnictides exhibit correlated electronic phenomena such as charge density waves and high-temperature superconductivity.^{1–3} The (re)discovery^{4,5} of single-layer graphene in 2004 by Novoselov

and Geim has shown that it is not only possible to exfoliate stable, single-atom or single-polyhedral-thick 2D materials from van der Waals solids, but that these materials can exhibit unique and fascinating physical properties. In single-layer graphene's band structure, the linear dispersion at the K point gives rise to novel phenomena, such as the anomalous room-temperature quantum Hall effect, and has opened up a new category of "Fermi-Dirac" physics. Even at one-atom-thick, graphene is a fantastic electronic and thermal conductor, and graphene-based materials have been proposed for a host of

* Address correspondence to goldberger@chemistry.ohio-state.edu.

Received for review January 18, 2013 and accepted March 6, 2013.

Published online March 06, 2013
10.1021/nn400280c

© 2013 American Chemical Society

applications ranging from transparent conductors to thermal interface materials to barristor transistor-like devices.^{6–8} Furthermore, as single-layer graphene is entirely surface area, its properties and reactivity profoundly depend on the substrate, its local electronic environment, and mechanical deformations.

Still, there exists an entire periodic table of crystalline solid-state materials each having different electronic, mechanical, and transport properties, and the possibility to create single-atom or few-atom polyhedral thick 2D layers from any material remains. It was shown decades ago by Frindt *et al.* that layered van der Waals materials, such as layered metal dichalcogenides, could be mechanically and chemically exfoliated into few and single layers.^{9,10} This early work focused on attempts to obtain and characterize these thin layers.^{9–13} Experiments probing transport¹¹ only scratched the surface of the unique properties these 2D materials exhibit. It was not until the recent surge of intense research on graphene that the general potential of 2D materials became apparent. Additionally, the past 8 years of graphene research has yielded many methods for synthesizing, transferring, detecting, characterizing, and manipulating the properties of layered van der Waals materials. Furthermore, novel synthetic methods including topotactic, solution-based, solvothermal, and UHV surface epitaxial approaches have unleashed the potential to create new van der Waals solids and single-layer-thick materials. These established methods have enabled the field of 2D materials beyond graphene to mature very quickly.

Many novel materials that had been initially considered to exist only in the realm of theory have been synthesized. These include groups IV and II–VI semiconductor analogues of graphene/graphane (the sp^2 /H-terminated sp^3 derivatives) such as silicene^{14–17} and germanane.¹⁸ Similar to graphene, the properties at the single layer are also distinct from the bulk. Furthermore, these 2D materials are useful building blocks that can be restacked and integrated into composites for a wide range of applications.

Herein, we present a forward-looking review article that discusses the state-of-the-art of 2D materials beyond graphene. Initially, we will outline the different chemical classes of 2D materials and discuss the various strategies to prepare single-layer and multi-layer assemblies in solution, on substrates, and on the wafer scale. Additionally, we present an experimental how-to guide for identifying and characterizing single-layer-thick materials, as well as outline emerging techniques that yield both local and global information. We describe the differences that occur in the electronic structure between the bulk and the single layer and discuss various methods of tuning the properties by manipulating the surface. Finally, we highlight the properties and advantages of single-, few-, and many-layer 2D materials in field-effect transistors, spin- and

VOCABULARY: two-dimensional material - a material in which the atomic organization and bond strength along two-dimensions are similar and much stronger than along a third dimension; **van der Waals solid** - a material whose crystal structure features neutral, single-atom-thick or polyhedral-thick layers of atoms with covalent or ionic bonding along two dimensions and van der Waals bonding along the third; **nanosheet** - stacked assembly or hybrid composite formed from single to many layers of two-dimensional materials; **graphane** - a single layer of a two-dimensional hexagonal network of sp^3 -bonded carbon atoms in which every carbon is bonded to a terminal hydrogen, alternatingly above and below the layer; **van der Waals epitaxy** - the growth of a thin layer on the surface of a substrate in which the material–substrate are held together by weak van der Waals forces.

valley-tronics, thermoelectrics, and topological insulators, among many other applications.

Structure and Synthesis of Two-Dimensional Materials. The reliable synthesis of single- and few-layer 2D materials is an essential first step for characterizing the layer-dependent changes in their properties, as well as providing pathways for their integration into a multitude of applications. In general, there are three main classes of materials that can be prepared as a single-atom or single-polyhedral-thick layer.

Classes of Single- and Few-Layer Two-Dimensional Materials. Layered van der Waals Solids. The most common class of crystalline structures that can be exfoliated as stable single layers are the layered van der Waals solids. These crystal structures feature neutral, single-atom-thick or polyhedral-thick layers of atoms that are covalently or ionically connected with their neighbors within each layer, whereas the layers are held together *via* van der Waals bonding along the third axis. The weak interlayer van der Waals energies (~ 40 – 70 meV) enable the facile exfoliation of these layers. The most common approaches for obtaining single- and few-layer-thick 2D materials from many of these solids include mechanical exfoliation of large crystals using “Scotch tape”, chemical exfoliation by dispersing in a solvent having the appropriate surface tension, and molecule/atom intercalation in order to exfoliate these layers and enable their dispersion in polar solvents. This mechanical exfoliation process has been used to prepare and study the properties of few-layer van der Waals materials, such as MoS_2 and $NbSe_2$, since the 1960s.^{9,11,19} The isolation of individual and few layers using mechanical exfoliation remains the most powerful approach for studying their properties since it is considerably less destructive than the other methods and has successfully been used to create large, $10\ \mu m$ single-layer flakes on a variety of substrates.

One of the most well-studied families of van der Waals solids is the layered metal chalcogenides (LMDCs), the most common being MoS_2 . Early transition metal

dichalcogenides with stoichiometry MX_2 ($\text{M} = \text{Ti, Zr, Hf, V, Nb, Ta, Re}$; $\text{X} = \text{S, Se, Te}$) crystallize into layered 2D structures in which hexagonally packed MX_6 octahedra (for d^0 , d^3 , and some d^1 metals) or trigonal prisms (for d^1 and d^2 metals) share edges with their six nearest MX_6 neighbors within each layer (Figure 1a).¹ There are over 30 different LMDCs which have many technologically interesting properties, and an emerging body of experimental work investigating the structure and properties of single- and few-layer-thick derivatives has evolved for many of these compounds (MoS_2 , WS_2 , and TiSe_2).^{20–22} Other families of van der Waals solids that have been exfoliated into single layers include hexagonal boron nitride,²³ vanadium oxide derivatives, and other chalcogenides including Bi_2Te_3 , Sb_2Te_3 , and $\beta\text{-FeSe}$.^{24,25} Many novel van der Waals compounds can be created *via* the topotactic deintercalation of precursor solids. For example, the layered CaGe_2 and CaSi_2 Zintl phases can be topochemically deintercalated in aqueous HCl to produce layered hydrogen-terminated or half-hydrogen-terminated/half-hydroxy-terminated GeH and $\text{SiH}_{0.5}(\text{OH})_{0.5}$, respectively (Figure 1b).^{18,26–28} These group IV graphane analogues^{29–32} are a particularly intriguing class of systems due to the possibility of utilizing covalent chemistry to modulate and tune the properties. As another example, recently, the exfoliation of metal carbides such as Ti_3AlC_2 using HF to produce neutral layers of $\text{Ti}_3\text{C}_2(\text{OH})_2$ has been demonstrated.³³ New layered van der Waals solids are constantly being discovered by the solid-state community. In 2012, ReN_2 was synthesized for the first time using high-pressure techniques and was found to have the MoS_2 crystal structure type.³⁴

Neutral, dimensionally reduced hybrid organic/inorganic van der Waals derivatives of nonlayered solids have also recently been discovered. Dimensional reduction refers to the creation of novel crystal structures of metal-anion (M-X) frameworks by the addition of a reagent that disrupts the polyhedral connectivity along one or more dimensions while retaining a degree of the metal coordination geometry and general polyhedral connectivity.³⁵ In these hybrid van der Waals solids, stoichiometric equivalents of neutral organic ligands bind to the metal and disrupt the M-X-M framework without changing the electron count and relative metal-anion radii. For example, it has been shown that almost every II–VI semiconductor that typically crystallizes into the three-dimensional sphalerite or wurtzite lattices, such as ZnS , ZnSe , and ZnTe , can be converted into atomically thin 2D crystalline frameworks when synthesized *via* solution-phase solvothermal techniques in the presence of alkylamine ligands.^{36–40} The bulk sphalerite or wurtzite structure consists of a corner-sharing metal-anion tetrahedral. These dimensionally reduced structures can be envisioned as a single (1–10) plane of corner-sharing

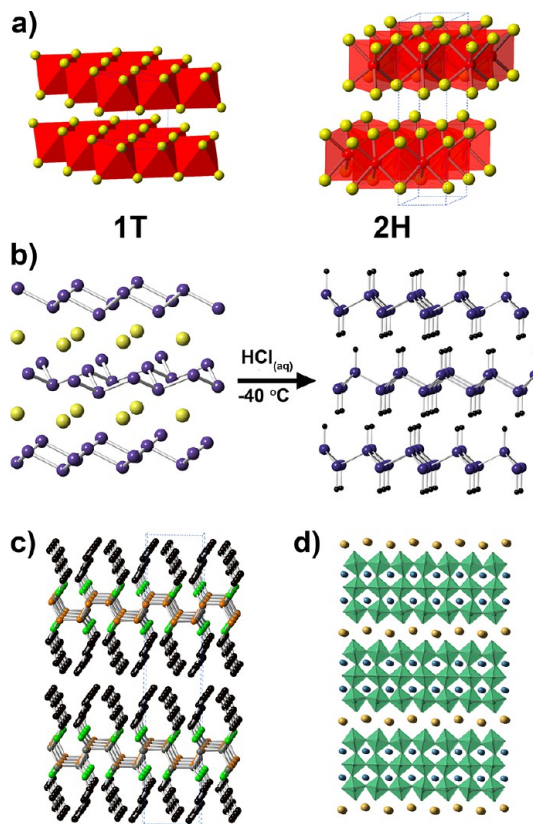


Figure 1. (a) Crystal structures of the 1T and 2H crystal structures of the MX_2 family (X = yellow sphere). The metal is in octahedral coordination in the 1T structure, and trigonal prismatic coordination in the two layers per unit cell 2H crystal structure. (b) Deintercalation of CaGe_2 in aqueous HCl at low temperatures results in GeH (calcium = yellow, germanium = purple, hydrogen = black). (c) Crystal structure of $\text{ZnSe}(\text{butylamine})$ (Zn = gray, Se = orange, N = green, C = black). (d) Crystal structure of $\text{KCa}_2\text{Nb}_3\text{O}_{10}$, a Ruddlesden–Popper perovskite phase that can be exfoliated upon replacing the K^+ cation (orange) with an organic cation.

metal-anion tetrahedra where every metal is bonded to three anions and capped with a short-chain alkylamine and every anion is bonded to three different metals (Figure 1c). The exfoliation into single-layer-thick derivatives of these hybrid materials, such as ZnSe , has been recently demonstrated.⁴¹

Layered Ionic Solids. The second class of materials that can be prepared as single or few layers features bulk crystal structures with *charged* 2D polyhedral layers that are typically held together with strongly electropositive cations or strongly electronegative anions such as halides, or OH^- . To enable their dispersion as single layers in solution, these cations/anions are typically exchanged with bulky organic cations/anions, such as tetrabutylammonium/dodecyl sulfate. These materials can then be easily dispersed onto substrates, with the majority of materials depositing as single to few layers. There are numerous examples of oxide materials that have been prepared this way including (1) cation-exchanged layers from Ruddlesden–Popper perovskite-type structures, such as $\text{KLn}_2\text{Ti}_3\text{O}_{10}$, KLnNb_2O_7 , $\text{RbLnTa}_2\text{O}_7$, and $\text{KCa}_2\text{Nb}_3\text{O}_{10}$

(Figure 1d)^{42–47} (Ln = lanthanide ion); (2) cation-exchanged layered metal oxides such as LiCoO₂ and Na₂Ti₃O₇;^{48,49} (3) halide- or hydroxide-exchanged layers derived from metal hydroxides, such as Ni(OH)_{2–x} or Eu(OH)_{2.5}Cl_{0.5}.^{50,51} Additionally, many neutral layered transition metal oxides such as MnO₂ can undergo changes in oxidation state and become protonated in aqueous acidic solutions.⁵² This proton can then be substituted for bulky organic cations. The observed thicknesses from atomic force microscopy (AFM) for these classes of materials are typically larger than their expected values due to the presence of hydration layers or intercalating ions, which results in a surface–sheet interface with a thickness between 0.5 and 1.0 nm. The lateral sizes of exfoliated layers from ionic materials typically depend on the size of the starting crystalline material, and single-layer flakes in the range of tens of micrometers have been observed.⁴⁸

Surface Growth of Nonlayered Materials. The deposition of materials on substrates offers the potential to grow and study the properties of single- to few-atom-thick materials beyond those existing as layered bulk crystals. For example, recently, it was demonstrated that monolayers of silicon deposited on Ag(111) or ZrB₂ organize into a puckered hexagonal graphene-like lattice with sp² bonding configuration.^{17,53} This silicene material shares a similar band structure to graphene; however, the interactions with the substrate induce a band gap opening at the K point. Additionally, ultrathin insulators such as Cu₂N,^{54,55} Al₂O₃,⁵⁶ NaCl,⁵⁷ MgO,⁵⁸ TiO₂,⁵⁹ and metal adlayers have been prepared in this fashion on metal substrates. Unlike exfoliation, the choice of substrate has been typically limited to metals due to the prevalence of STM as a characterization tool.

Solution-Phase Growth. Solution-phase methods such as solvothermal or colloidal growth reactions offer a facile production method to synthesize gram scale quantities of 2D materials with precise thicknesses and basal-plane sizes.^{60–64} Recently, general colloidal synthetic methods have been developed to prepare LMDCs such as TiS₂, VS₂, ZrS₂, HfS₂, NbS₂, TaS₂, TiSe₂, VSe₂, and NbSe₂ via the reaction of metal halides and carbon sulfide or elemental selenium in the presence of primary amines.⁶⁵ The colloidal materials typically range in lateral dimensions from 10 to 100 nm and have thicknesses from single sheets to tens of nanometers. As an example, TiS₂ nanosheets that have lateral lengths of 500 by 500 nm with thicknesses on the order of 5 nm have been created (Figure 2). These methods use abundant low-cost precursors and mild colloidal growth conditions.⁶⁶ However, strategies for controlling the thicknesses and lateral dimensions have yet to be established.

One of the key steps in using solution-phase methods to grow transition LMDCs is the generation of chalcogenide anions in the appropriate oxidation state (S^{2–}, Se^{2–}, and Te^{2–}). To grow sulfides, primary amines

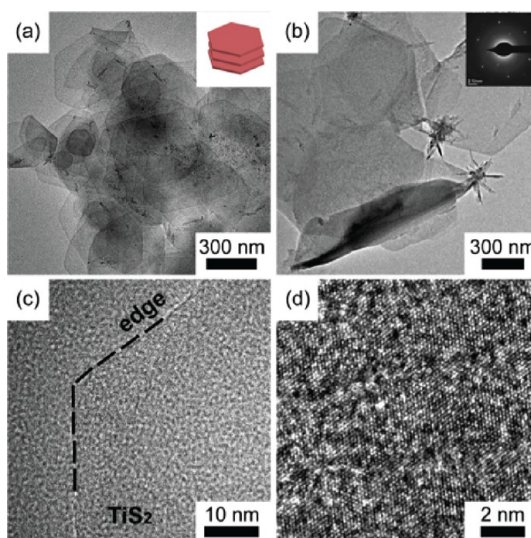


Figure 2. (a,b) Low-resolution TEM images of TiS₂ layers. The inset in (a) shows an image of multiple TiS₂ nanosheets, and the inset in (b) a selected area electron diffraction pattern of a single TiS₂ layer. (c,d) High-resolution TEM images showing the edge and basal plane of a single TiS₂ layers.⁶⁶

and sulfur are typical reactants because they form sulfur-containing alkylammonium polythioamine,⁶⁷ polythiobisamine,^{68,69} and alkylammonium polysulfide⁷⁰ complexes. These sulfur-containing species, in turn, exhibit favorable decomposition kinetics and produce H₂S when heated, which reacts with the metal precursor.

Vapor Deposition. Vapor deposition stands as an appealing, versatile synthetic strategy. However, the development of a controlled synthetic method of 2D materials such as 2D chalcogenides by vapor deposition requires a better understanding of the fundamentals involved. While vapor deposition has been extensively used for the growth of thin films and nanomaterials such as nanowires,⁷¹ nanotubes,⁷² and graphene,⁷³ knowledge obtained from these materials may not simply apply to 2D materials. Unlike typical nanomaterials whose growth is primarily governed by a catalyst, the vapor deposition growth of 2D chalcogenides is often noncatalytic.^{24,74,75} Without the dominance of catalysts, the growth of 2D nanosheets is subject to strong influences of many experimental parameters that may play only a negligible role in catalyzed growths. For example, the diffusion of source material vapor through the gas flow boundary layer strongly controls the vapor deposition growth of GeS nanosheets (Figure 3).⁷⁴

The growth of single-layer substrate-wide 2D materials is essential for commercialization and would also benefit fundamental studies of single-layer phenomena. The key to the preparation of substrate-wide single-layer van der Waals 2D materials and their heterojunctions is monolayer (ML) epitaxy. van der Waals forces have associated energies of 40–70 meV, which

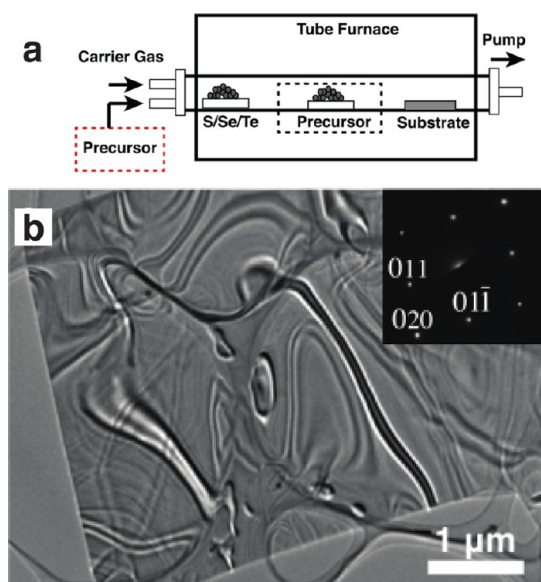


Figure 3. (a) Schematic illustration of experimental setup for synthesis by a noncatalytic vapor deposition process. The precursor vapor can be introduced from outside or generated inside the tube furnace. (b) TEM image of a typical GeS nanosheet. Inset is an electron diffraction pattern of the nanosheet.⁷⁴

are much smaller than covalent bonding energies of 200–6000 meV. We infer that epitaxy of crystalline 2D materials on crystalline substrates is defined by strong bonding at the reactive edges of the single-crystal domains of the material and weak interlayer forces between the sheets. This van der Waals epitaxy occurs between 2D sheets of the same material (homoepitaxy) as well as 2D sheets of different materials (heteroepitaxy). Because of the weak interlayer forces, epitaxy is possible even if there is significant lattice mismatch between the materials.^{25,75} The resulting heterojunctions do not suffer from the interfacial defects that are generated during 3D heteroepitaxy due to the large stresses generated by bent or broken interlayer bonds.^{76,77} van der Waals heteroepitaxy has also been shown to be possible with 3D substrates that have been suitably passivated.^{76,77} Table 1 shows a listing of crystalline 2D heterojunctions that have been produced using van der Waals epitaxy.

Large-Area CVD Growth of Graphene and Hexagonal Boron Nitride. It is worthwhile to re-evaluate the successful vapor deposition growth of single-layer graphene in order to understand the extent to which we can transfer these methods to the substrate-wide growth of other van der Waals systems. Thin carbon films were originally grown on single-crystal transition metals such as platinum by exposing the metal surface to a hydrocarbon at high temperature in ultrahigh vacuum (UHV) conditions.^{78–80} LEED patterns observed by the Somorjai group^{78–80} were assigned in 1969⁴ to being from single- and few-layer graphene (SLG and FLG, respectively). The formation of these graphene layers was later explained by the dissociation of the hydrocarbon on the metal surface, carbon diffusion into the bulk of the

TABLE 1. Two-dimensional Heterojunctions Produced by van der Waals Epitaxy

layer	substrate	ref
graphene	sapphire	322
C ₆₀	MoS ₂	323
MoS ₂	graphene	75
GaS	GaSe, Si(111)	324
GeS	SiO ₂ /Si	74
TaS ₂	mica	325
WS ₂	graphite	326,327
HfS ₂	WSe ₂	328
CdS	InSe/H-S(111)	329
SnS ₂	WSe ₂ , MoS ₂ , MoTe ₂ , GaSe, WSe ₂	330,331
SnSe ₂	SnS ₂ , WSe ₂ , MoS ₂ , MoTe ₂ , GaSe	330,331
Bi ₂ Se ₃	graphene/SiC, Si(111)	238,332
BiTe ₂ Se	h-BN	333
ZnSe	InSe, GaSe	334
MoSe ₂	SnS ₂ , MoS ₂ , GaAs(111)	335
GaSe	GaAs(111), Si(111)	336,337
NbSe ₂	mica, GaAs(111)	338
CdTe	MoSe ₂ , WSe ₂	339
PbTe	Si(111)	340

metal, and its segregation during cooling or by carbon supersaturation.^{81,82} There is an interest in synthetic approaches for the formation of large-area graphene, for basic research as well as a variety of applications, and this has driven the re-evaluation of FLG growth on transition metals by the diffusion–segregation technique. The growth of FLG on Ru,⁸³ Ir,⁸⁴ Co,^{85,86} Ni,^{73,81,82,87} Pt,⁸⁵ and Pd⁸⁵ by chemical vapor deposition (CVD) has been reported. Control of the quality and number of layers grown has proven challenging, and often inhomogeneous films are obtained. FLG was also achieved by the sublimation of silicon in SiC crystals.⁸⁸

The successful synthesis of SLG with high homogeneity and reproducibility was achieved in 2009 by low-pressure CVD on copper foils with methane as the carbon source.⁷³ Aspects of the growth kinetics and mechanisms were elucidated using an isotope-labeling technique in which the Cu is exposed sequentially to ¹³CH₄ and then normal methane.⁸⁹ ¹³C-labeled graphene can be readily distinguished from normal graphene by Raman spectroscopy and mapping (Figure 4a). A comparison of the growth of monolayer graphene and FLG on Cu *versus* Ni showed that the graphene growth on Cu is surface-mediated; that is, dissociation of the hydrocarbon followed by carbon species diffusion on the surface leads to nucleation, island growth, and finally completion of a monolayer.⁸⁹ This is rationalized by the extremely low carbon solubility in Cu even at the growth temperature of about 1040 °C that inhibits the diffusion of C into the bulk Cu, making Cu foil an excellent substrate for growth of large-area SLG. Kinetic studies on the growth of graphene led to the conclusion that the graphene grain size could be increased by raising the growth temperature and

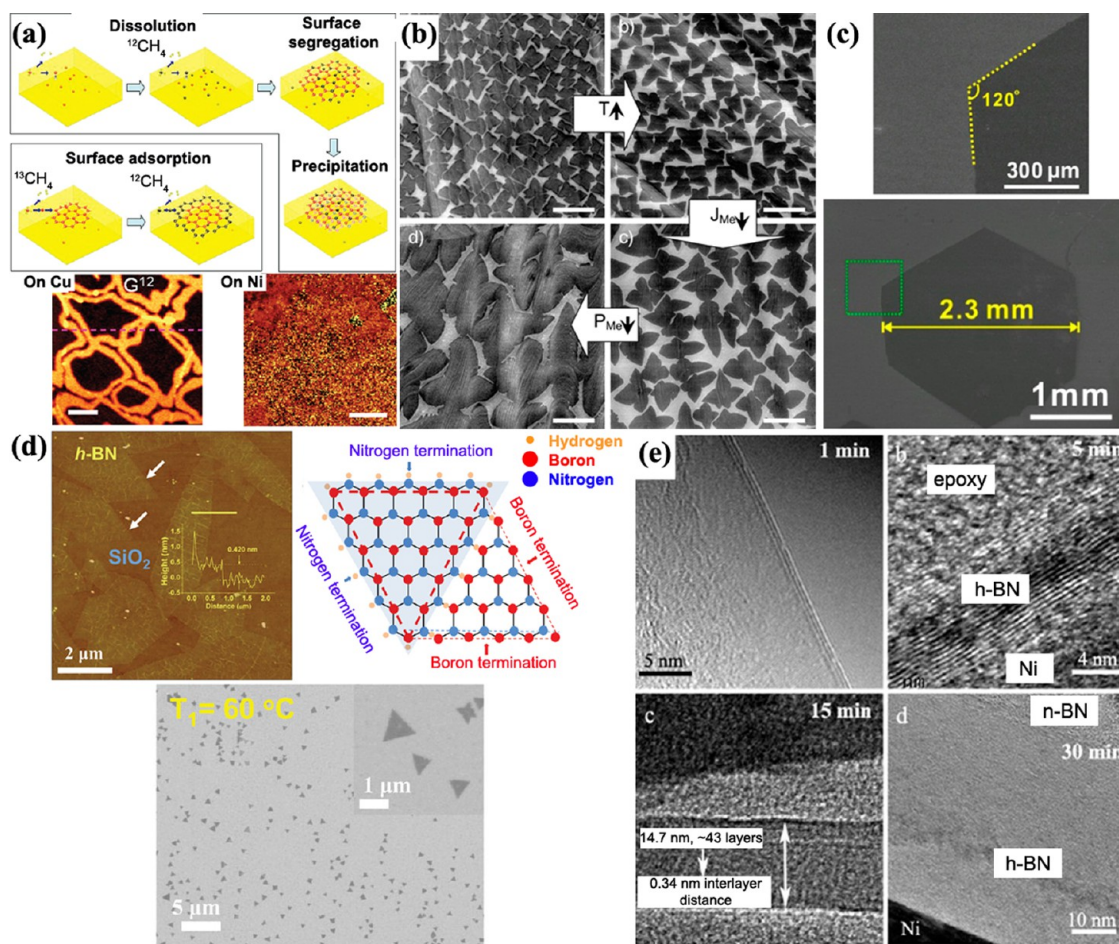


Figure 4. (a) Schematic illustration showing the dissociation–dissolution–segregation on Ni and the surface-mediated growth of monolayer graphene on Cu. The Raman mapping of the G band for graphene grown on Cu (bottom left) shows graphene areas enriched with ^{13}C (dark) and normal C (bright); note that the distribution of ^{13}C is essentially random for the film grown on the Ni foil (bottom right); scale bars are $5\ \mu\text{m}$. (b) Increasing the domain size by raising the temperature (T) and lowering both the precursor gas flow (J_{Me}) and the methane partial pressure (P_{Me}) as compared to an earlier protocol, SEM images; scale bars are $10\ \mu\text{m}$.⁹¹ (c) SEM images showing further increase of the graphene domain size which was attributed to controlling the surface roughness of the Cu foils.⁹³ (d) AFM and SEM images showing submonolayer h-BN transferred to a SiO₂/Si and Cu foil, respectively, in which triangular domains can be observed. The atomic model for such domains is depicted on the right.²³ (e) Control of the number of h-BN layers on Ni foils by control of the reaction time. TEM images for samples grown for 1, 5, 15, and 30 min.⁹⁸

reducing the partial pressure of the hydrocarbon, and grain size was thereby increased, at first, from a few micrometers to tens of micrometers.⁹⁰ The domain size of SLG has since been increased to several hundred micrometers^{91,92} and even millimeters⁹³ (Figure 4c). One measure of graphene “quality” is the magnitude of the carrier mobility, and larger grain size has been correlated with higher carrier mobility values.^{90,93}

“Good” conditions to grow SLG include (1) hydrocarbon dissociation (catalytic or thermal); (2) a catalyst favoring growth of graphene; and (3) nucleation, growth, and completion of the monolayer film by having all reactions occurring on the surface of the substrate. Indeed, SLG was shown to grow in UHV conditions on single-crystal metals with high carbon solubility^{4,82} and more recently by low-pressure CVD on Ni films⁹⁴ by controlling the kinetic factors during the growth and, in particular, having the reaction occur

only on the metal substrate surface. Other relevant parameters are the sticking coefficient of the carbon species on the metal surface and these species’ ability to diffuse on the surface.

In contrast to graphene, other layered systems are composed of two or more elements, making the synthesis more complex. Hexagonal boron nitride (h-BN) might be the most studied layered material after graphene, although reports on the CVD synthesis of MoS₂ are emerging.⁹⁵ The synthesis of single- and few-layer h-BN was achieved first in UHV CVD systems on single-crystal metals.⁹⁶ Recently, the synthesis of single-layer h-BN and few-layer h-BN was reported in CVD systems using solid^{23,97} and gaseous precursors.⁹⁸ Submonolayer domains on Cu foils were achieved using very low partial pressure of ammonia borane²³ (Figure 4d), while control over the number of layers was achieved using diborane and ammonia on Ni foils,⁹⁸ as

depicted in Figure 4e. Despite such achievements, the growth mechanism for h-BN remains unclear. The growth of SLG was significantly improved in only a few years by understanding some of the key parameters for growth. Can we apply similar methodologies to the growth of single or multiple layers of other layered materials? It calls for further nucleation and growth studies as well as an adequate set of characterization tools comparable to those used to characterize graphene.

Multilayer Assemblies. As will be discussed later, there are numerous applications for multilayer assemblies and hybrid composites from single- to many-layer (thickness $<1\ \mu\text{m}$) 2D materials, which we will define as nanosheets. The most common methods for assembly rely on solution processing. Colloidally dispersed nanosheets can be self-assembled into useful constructions like porous solids, nanostructured thin films, hybrid polymer–inorganic nanocomposites, superlattices, and other hierarchical structures.^{99–101} Effective wet-processing assembly techniques are electrostatic layer-by-layer assembly,^{102–105} Langmuir–Blodgett (LB),^{106–108} flocculation,^{12,109} and electrostatic self-assembly deposition (ESD).^{110,111} In these methods, the nanosheets are colloidally dispersed and then either deposited directly onto a substrate (layer-by-layer, LB) or aggregated into a nanocomposite in solution (flocculation, ESD). Other techniques to create single- and few-layer nanosheet assemblies during the gas-phase growth such as “chemical blowing” are emerging.^{112,113}

The layer-by-layer method is one of the most precise approaches for constructing multilayered films with controlled architecture, composition, and thickness. This method employs polyelectrolytes absorbed onto the sheets and substrates to enhance the absorption of charged nanosheets.^{102,109,114} Nanosheet multilayer assemblies are formed by alternately dipping substrates in colloidal suspensions of charged nanosheets and in aqueous solutions of polyelectrolytes having the opposite charge.¹⁰¹ This technique has successfully been used to prepare interstratified composite materials with two separate nanosheet materials (superlattices) by sequential absorption of each layer.¹⁰⁹

Electrostatic interactions between cations and nanosheets at the air/water interface can allow nanosheets to float, thus enabling use of conventional LB procedures.^{63,115,116} In this technique, a floating monolayer of nanosheets is formed in a Langmuir trough on a fluid surface, which is then horizontally compressed and then transferred onto a substrate by vertical dipping. The LB techniques can be used to deposit nearly perfect monolayer and multilayer films that are atomically smooth, high density, and without pinholes. For example, the LB method has been employed to produce single- and several-nanometer-thick titano niobate and titanate layers that have a clean interface with the substrate.^{117,118}

Recent work has demonstrated a new method to create millimeter-scale stacks of nanosheet assemblies

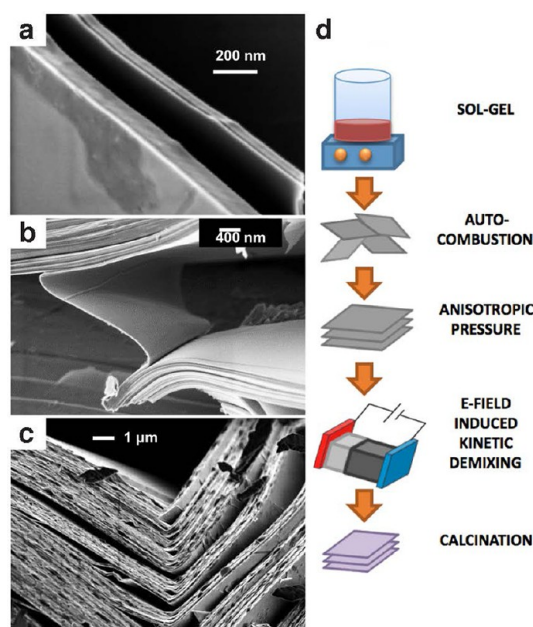


Figure 5. (a) SEM images of two individual $\text{Na}_{0.7}\text{CoO}_2$ metal-oxide nanosheets. (b,c) Nanosheets displaying extreme ductility after mechanical bending is applied. (d) Synthetic procedure involving sol–gel solvation of metal ions, pyrolysis resulting in flakes, application of pressure to compress and align flakes, electric-field-induced kinetic demixing of Na^+ ions, and calcination into nanocomposites of stacked nanosheets.¹¹⁹

with aligned layers. The method involves the sol–gel creation of 2D amorphous flakes, followed by pressurization-induced alignment of the flakes, electric-field-induced kinetic demixing, and finally calcination into stacks of single-crystalline sheets (Figure 5d).¹¹⁹ The kinetic demixing is the critical component to forming millimeter-length nanosheets: the kinetic demixing locally concentrates the mobile cations, which then diffuse laterally outward during calcination, forming the nanosheet stacks. For example, this method has produced Na_xCoO_2 nanosheet nanocomposites containing tens of thousands of self-assembled $\sim 20\ \text{nm}$ thick nanosheets that display interesting properties, such as extreme ductility, and can be bent up to 180° (Figure 5a–c) despite being composed from a ceramic.¹¹⁹ In the nanocomposites, the individual nanosheets are oriented to each other with turbostratic axial alignment. After exfoliation, the nanosheet lateral lengths can measure $350\ \mu\text{m}$. This procedure should be applicable to other ternary layered metal oxides.

Characterization of Two-Dimensional Materials. Probing the molecular and vibrational structure of 2D materials is inherently challenging due to the small sample size. However, numerous methods have been developed to enable their identification and characterization. In this section, we will provide a standard how-to guide for studying single-layer-thick materials. Furthermore, we will highlight emerging, less commonly used techniques that have the potential to simultaneously merge

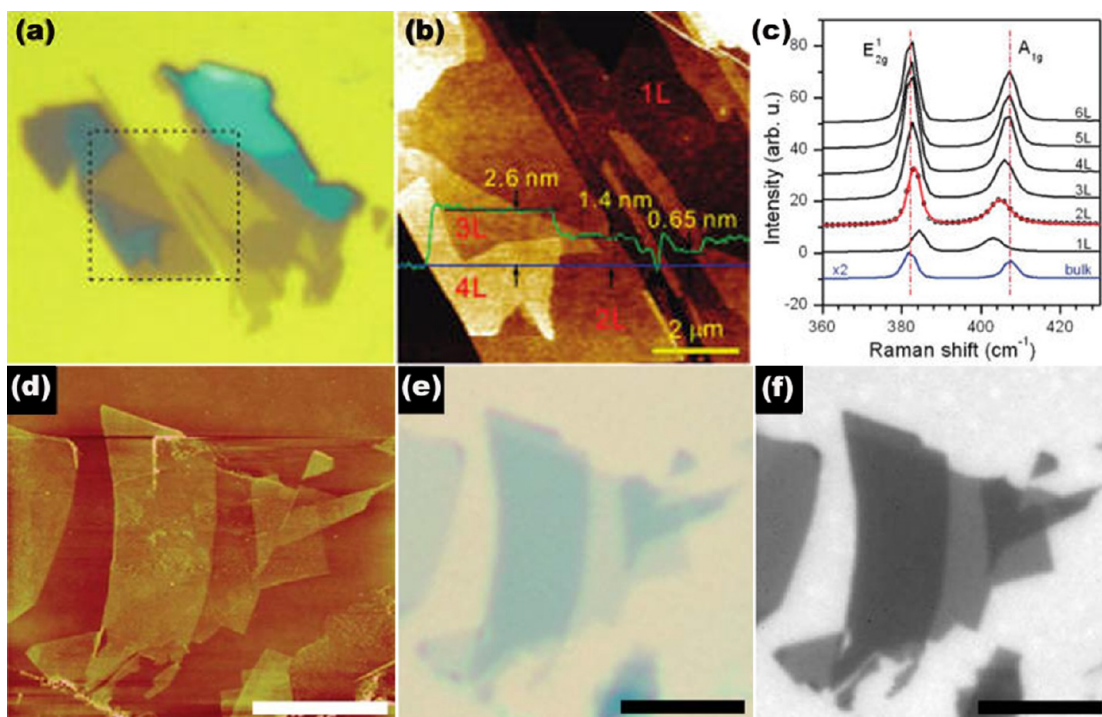


Figure 6. (a) Optical micrograph of thin films of MoS₂.¹⁵⁰ (b) AFM of MoS₂.¹⁵⁰ (c) Raman spectra of single-layer, few-layer, and bulk MoS₂ films.¹⁵⁰ (d) AFM of graphene.¹²⁶ (e) optical micrograph of graphene.¹²⁶ (f) FQM image of graphene using PVP/fluorescein.¹²⁶ Scale bars are 10 μ m.

structural or spectroscopic information with properties at the local scale.

The first challenge in single-layer characterization is single-layer preparation and detection. Mechanical exfoliation from bulk crystals is typically the simplest method for transferring 2D sheets of layered van der Waals solids such as graphene,^{5,20,120,121} metal chalcogenides,¹²² and GeH¹⁸ to any substrate. Exfoliation typically produces 10 μ m sized flakes ranging in thickness from single to few layers. Optical microscopy is initially the most powerful high-throughput method for initially identifying single- and multiple-layer flakes.^{20,58,122,123} Dielectric-coated SiO₂/Si substrates are the most common substrates used to visualize and locate single and few layers (Figure 6a,e,f). The color of the dielectric-coated wafer depends on an interference effect from reflection off of the two surfaces of the dielectric. Single- and few-layer flakes on the surface of the dielectric modify the interference and create a color contrast between the flake and the substrate.^{123,124} For optimal contrast, the thickness of the dielectric coating needs to be within 5 nm of the ideal value. However, since the index of refraction of many novel materials is unknown, it is often necessary to first experimentally exfoliate onto a range of substrates having different dielectric thicknesses to initially determine the optimal thickness.

Visualizing single layers on other substrates without the need for interference methods has also been explored. Some metal dichalcogenides (MoS₂, WS₂)

have direct band gaps only as single layers, enabling their direct visualization by fluorescence microscopy.¹²⁵ However, as the number of layers increases, these materials' band gaps become indirect, significantly reducing their fluorescence.

Fluorescence Quenching Microscopy (FQM) uses an organic fluorophore whose fluorescence is quenched in the presence of single- or few-layer sheets (Figure 6f). Many 2D materials feature either low enough band gaps or the appropriate band alignment to quench nearby fluorophores *via* a FRET mechanism or charge transfer mechanism. One can locate single layers of 2D materials on a substrate by monitoring the reduction in fluorescence intensity of a thin fluorophore layer that was spun-coat on top.^{126–128}

AFM is a powerful technique to determine layer thickness (Figure 6b,d) with a precision of 5%.^{114,118,129} However, discrepancies arise from differences in the interactions of the tip with the sample and substrate.¹³⁰ For example, the thickness of a single layer can be better determined by measuring the height of a second layer on a first layer, rather than the height between a single layer and the substrate because in the former the tip–layer interactions are constant. To control these differences and obtain the most accurate height profile of a single layer, one must first optimize the tip–surface distance to exclude any hysteretic artifacts.¹³⁰

Raman Spectroscopy is a useful method for fingerprinting a material and layer-dependent changes of the vibrational structure (Figure 6c). It is necessary to

use low power (e.g., 16 kW/cm² for Bi₂Te₃,¹³¹ or 40 kW/cm² for GeH) when obtaining Raman spectra of single layers to prevent sample decomposition. The Stokes/anti-Stokes peak ratio can be used to determine the local temperature.¹³² Raman spectra can also detect vibrational modes that are active due to symmetry breaking in single-layer films and enhanced vibrations in out-of-plane modes when the single layer is suspended.¹³¹ When varying the layer number between bulk, few, and single layers, the Raman spectra differ in spectral width and intensity due to differing interlayer interactions.^{122,129} Substrates that have vibrational modes that overlap with those in the material of interest should be avoided. Vibrational spectroscopy, in general, and Raman spectroscopy, in particular, could be used to detect isotopic-enriched 2D materials to study the growth mechanism as demonstrated and thus be used to study the growth mechanism.⁸⁹

Transmission Electron Microscopy (TEM) can provide detailed information on the nature of crystallinity, layer sizes, interlayer stacking relationships, and elemental composition (Figure 7a,b).^{63,114,119,122,133–135} In the case of graphene, selected area electron diffraction can distinguish between monolayer and multilayer graphene when the intensity ratio of the (100) to (110) diffraction spots is larger or smaller than 1, respectively. This deviation in diffraction intensity can also distinguish between single- and multilayer flakes of other 2D materials when there is a change in interlayer registration. Recent advances have shown that dark-field microscopy can quantitatively determine the layer number and stacking order of multilayer graphene.¹³⁶ Scanning transmission electron microscopy (STEM), using high-angle annular dark-field detector coupled with electron energy loss spectroscopy can be used to visualize individual atoms in an isolated layer. Here a sub-angstrom electron beam is rastered across a sample and is scattered when it hits a particular atom. Figure 7c shows a STEM image of carbon and oxygen substitutions in a single layer of boron nitride. Low accelerating voltages (<60 keV) are often necessary to minimize beam damage.

Scanning Tunneling Microscopy (STM) is a probe-based technique that can measure the electronic and topographic structure of single-atom-thick materials and can manipulate single atoms at specific points in order to build and characterize nanostructures that are well isolated from the substrate (Figure 7d). Examples include STM studies of the unusual cyclotron quantization in graphene,^{137,138} as well as characterization of MoS₂ nanoislands¹³⁹ and BN.¹⁴⁰ Recent focus has shifted toward studies of adsorbates and defects, including metal adatoms on graphene^{141,142} and h-BN^{143,144} and molecules on MoS₂.¹⁴⁵ Due to the challenge of aligning a particular region of the substrate with the remote STM tip, the most commonly studied samples are epitaxially grown. Near-field tip-enhanced Raman

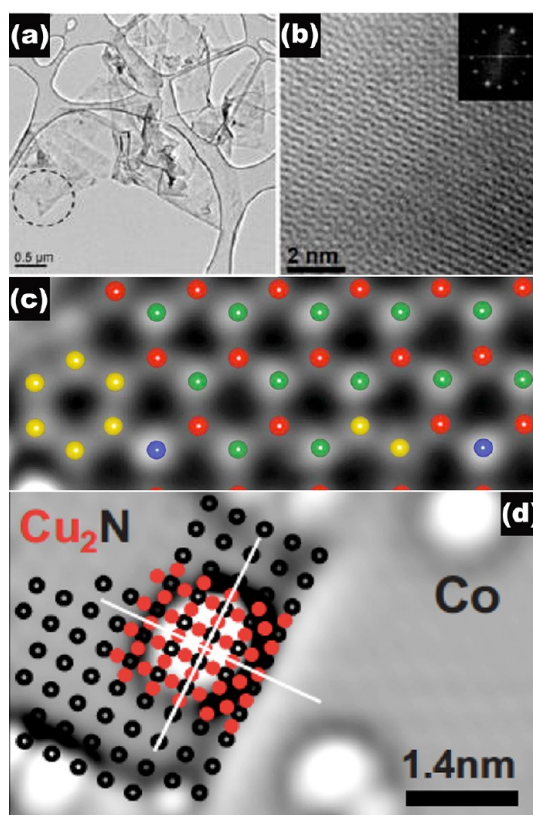


Figure 7. (a) Low-resolution TEM and (b) high-resolution TEM of a 2D WS₂ TEM island folded. Inset: Fast Fourier transform pattern.¹³⁵ (c) STEM image of a single BN layer containing C and O substitutional impurities overlaid on the corresponding part of the experimental image. Red, B; yellow, C; green, N; blue, O.³¹⁷ Reprinted with permission from ref 317. Copyright 2000 Nature Publishing Group. (d) STM image showing Co atoms adsorbed on Cu(100) and Cu₂N (0.1 V, 50 pA). The image was Laplace and Gaussian filtered to emphasize contrast. Open (closed) symbols denote N (Cu) sites within the Cu₂N island.³¹⁸

spectroscopy (TERS), in which an AFM or STM tip is coated with Au or Ag to enhance the local Raman spectra, has proven to be a powerful combined spectroscopic and imaging technique and, for example, has been used to identify defects and grain boundaries.^{4,5}

X-ray Diffraction (XRD)—both small-angle X-ray scattering (SAXS) and wide-angle XRD—can supply information about the unit cell structure and constituents, the sheet thickness and lateral dimensions, and the arrangement of restacked nanosheets. SAXS provides information about inter-nanosheet stacking since these peaks occur at lower angles.⁶³ By simulating the SAXS pattern, the stacking direction, sheet thickness, and distance between the sheets (from ligands or absorbed molecules) can be determined. For instance, patterns of wet colloidal aggregates of nanosheets and dried aggregates of nanosheets will display different XRD patterns: layer-to-layer registry can be disturbed for wet colloidal aggregates, while in-plane lattice planes are maintained, suggesting isolated nanosheets (Figure 8).^{111,146} For dried

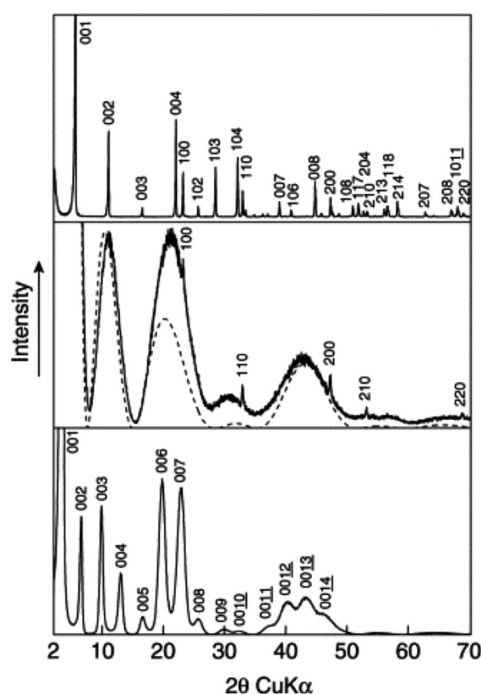


Figure 8. XRD patterns of niobate nanosheets of (top) bulk, (middle) (solid line) wet aggregates of nanosheets and (dashed line) calculated diffraction pattern for a single layer, (bottom) and dried aggregates of nanosheets.¹⁴⁶ Reprinted with permission from ref 146. Copyright 2002 Elsevier.

nanosheets, the presence of low-angle basal reflections in the pattern indicates an ordered arrangement of restacked nanosheets along the stacking axis, and likewise, the absence of intense basal reflections indicates random orientations for aggregated nanosheets.¹¹¹ The orientation of films on substrates favors the alignment of the thin axis. Broadening signatures of specific peaks under this orientation can indicate the thin axis.¹⁴⁷ To gain more insight, the nanosheet XRD pattern can be modeled by the structure factor, the Lorentz polarization factor, the Laue interference function, and the temperature factor.^{114,146} Structure factors for single and multiple layers can be calculated assuming atomic positions, unit cell structure, and orientation to a substrate.¹¹⁴ Results of this modeling can help determine the fundamental units of the nanosheets (e.g., atomic make up of termination layers), the spacing between sheets, and if the nanosheets are restacked. In-plane XRD can be used successfully to observe hk reflections (if l is the thickness axis) of the nanosheets' 2D unit cell.^{114,119} This is a useful method to observe missing peaks from the naturally textured orientation of nanosheets on a substrate. Unit cell parameters can be extracted from refinements of these data and compared to bulk values.

Characterization Opportunities. The development and implementation of new characterization techniques that can rapidly and nondestructively probe the atomic structure, defects, and properties of single-layer materials is necessary to advance the field. Since the

electronic properties of materials are often dominated by minority defects, the discovery, availability, and implementation of techniques that can identify minority species, defects, and edge states, such as next-generation aberration-corrected STEM as well as STM, will prove incredibly valuable. The emergence of combined spectroscopic and imaging techniques such as AFM-TERS can significantly aid in the identification and characterization of single-layer-thick sheets while minimizing substrate signals. Furthermore, to refine the growth of high-quality single-layer materials for electronic applications, the implementation of feedback loops between synthesis and device fabrication will be necessary.

Properties, Integration, and Devices. The unique qualities of 2D materials, such as their reduced dimensionality and symmetry, lead to the appearance of phenomena that are very different from those of their bulk material counterparts. This difference is perhaps most glaring in the transformation of the band structure as the single layer is approached. Additionally, since a 2D material is entirely made up of its surface, the interface between the surface and the substrate and the presence of adatoms and defects can dramatically alter the material's inherent properties. The two-dimensional nature of these materials also plays an entirely mechanical role as they are inherently flexible, strong, and extremely thin. These materials exhibit other unique and potentially useful properties including high electron mobilities, topologically protected states, tunable band structures, and high thermal conductivities. The development of 2D materials is expected to improve current device technology, and their novel transport and topological properties might provide additional opportunities for spintronic devices and quantum computing.¹⁴⁸ Even multilayer assemblies of 2D materials have a broad base of potential applications including batteries, supercapacitors, and p-n junctions. This section provides a detailed overview of the novel properties of 2D materials beyond graphene and discusses their potential for device applications and integration.

Changes in Electronic Structure at the Single Layer: *MoS₂*, a Case Study. The layered metal dichalcogenides (LMDCs) constitute one of the most studied families of van der Waals solids beyond graphite.¹⁴⁸ These materials display remarkably diverse electronic properties, ranging from metals to semiconductors to insulators. They also exhibit interesting strongly correlated electron phenomena, such as charge density waves and superconductivity. Among them, molybdenum disulfide (MoS_2 ; semiconductor), has attracted particular attention. Several distinctive properties, related both to its optical^{149–161} and transport characteristics,^{20,148,162–173} have been demonstrated in MoS_2 at the mono- and few-layer level. Examples of these properties include the existence of a direct gap,^{125,149} unlike the bulk material, with strong excitonic effects¹⁵⁶ and the possibility of

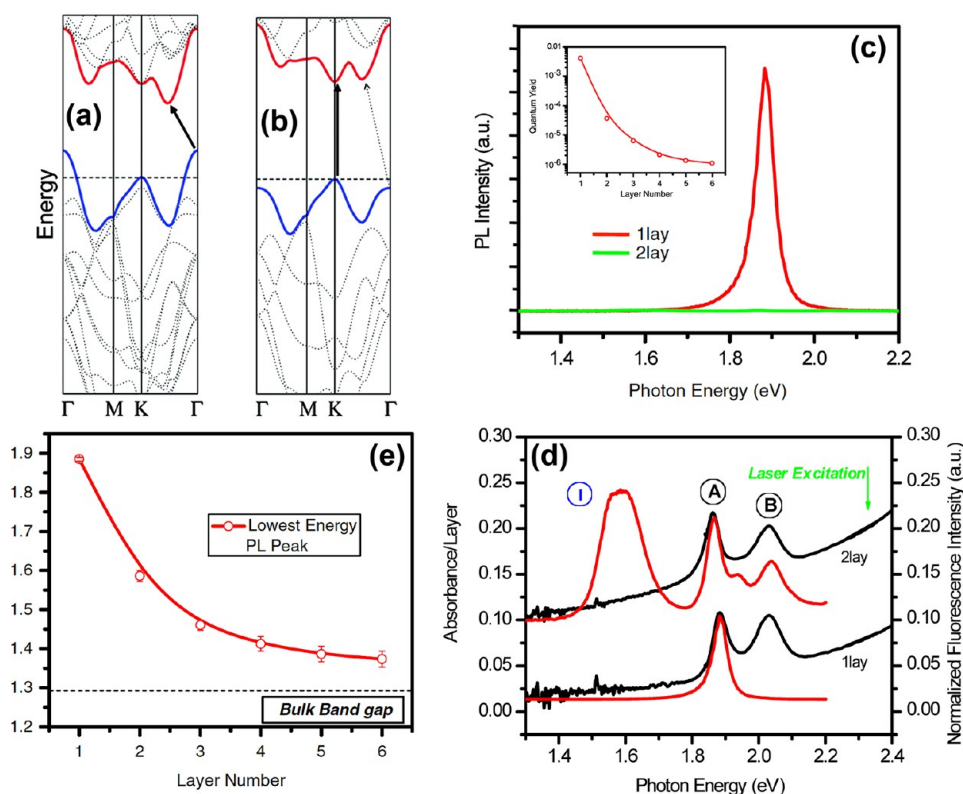


Figure 9. Calculated band structures of (a) bulk and (b) monolayer MoS_2 .¹²⁵ The solid arrows indicate the lowest-energy transitions. (c) PL spectra for mono- and bilayer MoS_2 samples. Inset: PL quantum yield of thin layers of MoS_2 for number of layers $N = 1-6$ in log scale. (d) Absorption spectra (left axis) normalized by the layer number N in the photon energy range from 1.3 to 2.4 eV for mono- and bilayer MoS_2 . The corresponding PL spectra (right axis, normalized by the intensity of the peak (A) are included for comparison. The spectra are displaced along the vertical axis for clarity. (e) Band gap energy of thin layers of MoS_2 for $N = 1-6$. The band gap values were inferred from the energy of the indirect gap PL feature I for $N = 2-6$ and from the energy of the PL peak A for $N = 1$. As a reference, the (indirect) band gap energy of bulk MoS_2 is shown as dashed line.¹⁴⁹

full control of the valley and spin occupation by optical pumping with circularly polarized light.^{153–155,158} MoS_2 has also been shown to yield field-effect transistors with very high current on–off ratios at monolayer thickness¹⁶³ and to function within a vertical graphene– MoS_2 –graphene tunneling transistor structure.¹⁷¹ These properties, in combination with the promise of synthesis of large-area high-quality samples (notably by recently developed CVD methods^{174,175}), suggest interesting possibilities for applications of this and related materials in electronics and optoelectronics. Here we summarize some of the recent progress in understanding the electronic properties of ultrathin MoS_2 layers.

The overall physical structure of the MoS_2 monolayer is similar to that of the graphene honeycomb lattice. For MoS_2 , however, the A and B sublattices, rather than both being occupied by C atoms, are occupied either by Mo atoms or by a pair of S atoms (Figure 12c), with the entire MoS_2 monolayer structure forming a triple layer of atoms. The difference between the A and B sublattices lifts the degeneracy in the electronic structure at the K (K') point in the Brillouin zone. This degeneracy is responsible for the distinctive Dirac cone dispersion relation in graphene. In contrast, in monolayer MoS_2 , a substantial energy gap is present.

The bulk MoS_2 crystal, consisting of MoS_2 monolayers arranged with Bernal stacking, is known to be an indirect gap semiconductor, with a band gap of 1.29 eV.¹⁷⁶ The calculated band structure for bulk MoS_2 shows that the valence and conduction band extrema occur away from the K (K') point (Figure 9a).¹²⁵ Through characterization by absorption, photoluminescence (PL), and photoconductivity spectroscopy (Figure 9c–e) as a function of thickness, Mak and co-workers¹⁴⁹ have traced the effect of quantum confinement on the electronic structure of MoS_2 layers. With decreasing thickness, the indirect band gap, which lies below the direct gap in the bulk material, shifts upward in energy by more than 0.6 eV. This leads to a crossover to a direct gap material in the limit of monolayer thickness since the electronic states near the K point are more localized within the layer and shift up in energy only modestly with decreasing layer thickness (Figure 9a,b). The result of this crossover in the band structure is the emergence of bright photoluminescence, which is absent for thicker films, in the monolayer material^{125,149} (Figure 9c). The direct gap character of monolayer MoS_2 has also been confirmed by *ab initio* calculations.^{125,177–181}

The ability to control the material's electronic structure through the sample thickness is not unique to MoS_2 .

Similar changes in the electronic band structure as a function of sample thickness have been predicted for other semiconducting LMDCs compounds MX_2 ($\text{M} = \text{Mo}, \text{W}$ and $\text{X} = \text{S}, \text{Se}, \text{Te}$).¹⁸² Furthermore, recent calculations have shown that the electronic and optical properties of monolayer and few-layer MoS_2 can be controlled through strain engineering.^{183–186}

Another important aspect of the properties of 2D semiconducting LMDCs such as MoS_2 is the important role of many-body electronic interactions. In particular, the optical properties are dominated by excitonic transitions. The enhanced Coulomb interactions existing in these materials can be attributed to reduced dielectric screening in these atomically thin systems. The absorption spectrum of the undoped MoS_2 monolayer (Figure 9d) shows pronounced absorption peaks from excitonic transitions, rather than the steps that would be expected for absorption arising from band-to-band transitions in a 2D system with a direct gap. The two features, known as the A (~ 1.9 eV) and B (~ 2.1 eV) excitons,^{125,149,187} arise from transitions from the two highest-lying spin-split valence bands to the lowest conduction bands.

The influence of doping on the optical properties of monolayer MoS_2 has been studied recently by Mak *et al.* using FET structures¹⁵⁶ for electrostatic control of the doping level. By analyzing the absorption and emission line shapes at low temperature, Mak *et al.* have identified, in addition to the presence of the usual neutral excitons, negative trions, quasi-particles composed of two electrons and a hole. The trion binding energy has been determined to be ~ 20 meV, which far exceeds that observed in conventional 2D semiconductor quantum wells and renders trions significant even at room temperature. Similar phenomena have also recently been observed in MoSe_2 FETs by Ross *et al.*¹⁵⁷

Because of symmetry, crystals frequently have independent, degenerate valleys in the conduction or valence band. Access to this so-called “valley” degree of freedom has attracted interest both from the point of view of fundamental physics and a possible new control variable for new classes of electronic devices, commonly called “valley-tronics” and discussed in more detail below. To date, however, it has proven difficult to selectively populate a given valley to produce valley polarization. MoS_2 monolayers with a direct energy gap at the K and K' points in the Brillouin zone have recently been predicted to be suitable for the control of valley population using optical pumping with circularly polarized light.^{154,188} Because of the broken inversion symmetry, strong spin–orbit interactions split the spin-degenerate valence bands by ~ 160 meV in MoS_2 monolayers. This broken spin degeneracy, in combination with time-reversal symmetry, implies that the valley and spin of the valence bands are inherently coupled. When optical transitions between the upper valence band and the conduction band

(corresponding to the A exciton) are induced by circularly polarized photons, excitation occurs only at either the K or K' valley, depending on the helicity of the light. This excitation process, because of the coupled valley and spin degree of freedom, also gives rise to photo-generated particles of a well-defined spin state. These theoretical predictions have been recently verified by several experimental groups^{153–155,158} through a demonstration of the retention of the circular polarization state of light emission induced by resonant excitation with circularly polarized light. The important role of inversion symmetry in establishing valley polarization was further confirmed by a comparison of the behavior of MoS_2 bilayers in which inversion symmetry, unlike for the case of the monolayer, is present. More general discussion of 2D materials for spin- and valley-tronics is provided in later sections of this review.

Edge Effects on the Electronic Structure. As we discuss in the previous section, LMDCs exhibit novel physicochemical properties when the bulk (3D) form is reduced to a monolayer (2D). The most notorious change is related to the electronic band structure, which can change from an indirect band gap in 3D to a direct band gap in a 2D monolayer.^{135,149} If the monolayer has finite lateral dimensions, contributions from the edges might become important and new phenomena are expected.^{135,189} Although a monolayer of LMDCs is actually composed of three atomic layers in which each layer of metal atoms is sandwiched between two layers of chalcogen atoms (X–M–X), the projection in the plane exhibits a hexagonal or honeycomb-like crystal structure similar to graphene; hence the edge terminations can be zigzag, armchair, chiral, or a mixture of these types.

Both the structural and chemical terminations of the edge are crucial to determine the local physicochemical properties of these systems. First principles calculations have predicted that diverse edge passivation in metal dichalcogenides could produce different spins states that modify the edge electronic and magnetic properties.^{135,189,190} In addition, high spin density could be localized surrounding metal vacancies.¹⁹¹ The experimental exploration of edges in inorganic 2D materials is still at an early stage. From the experimental point of view, triangular clusters of MoS_2 on Au substrates have been studied by STM,^{139,192,193} revealing metallic electronic states localized close to the edges. For perfect continuous edges, those metallic states can be viewed as one-dimensional conducting wires.¹⁹² The same group studied the size dependence of the cluster morphology and electronic structure and consistently found sulfur-terminated edges in single-layer clusters.¹³⁹ Enhanced catalytic activity has also been correlated with the density of edge sites in MoS_2 2D clusters.¹⁹⁴

To date, MoS_2 has been the testing ground for many experiments in monolayers of metal

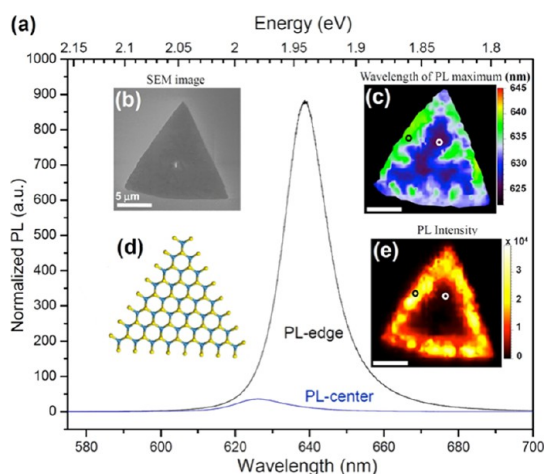


Figure 10. (a) Room-temperature PL spectra at two different positions (small circles in c and e) on the island shown in (b). (b) SEM images of a large WS₂ triangular island. (c,e) Corresponding micro-PL mappings of the PL peak position and the absolute intensity at the peak maximum, respectively. (d) Top-view atomistic model of a small WS₂ cluster with sulfur-saturated zigzag edges.¹³⁵

dichalcogenides.^{135,139,149,150,152,155,163,173,174,194,199–202} However, other compounds of this family are also good candidates to study new and exciting properties.^{135,191,199–202} Recently, the optical behavior of WS₂ triangular monolayers was investigated by Raman spectroscopy and micro-PL.¹³⁵ Monolayers of WS₂ exhibited a single PL peak between 1.9 and 2.0 eV, corresponding to a 2D exciton associated with the direct band gap transition. A remarkable enhancement of the PL intensity was observed in regions close to the edges of the 2D triangular clusters (Figure 10a). PL mappings of the WS₂ triangular island (Figure 10b) showing the peak position and absolute maximum intensity, respectively, are shown in Figure 10c,e. In general, the spectrum closer to the edge shows both a significantly stronger PL signal when compared to the central region, as well as a red shift of the PL peak. TEM analysis revealed that the triangular islands possess mainly zigzag edges, and the synthesis conditions provided a sulfur-rich environment. Determining the exact mechanism for PL enhancement demands a one-to-one correlation between the chemical structure of the edge and its optical response. The main challenge consists of implementing experiments that reveal the exciton dynamics, such as temperature-dependent PL and/or time-resolved PL, with spatial resolution of the order of tens of nanometers.

Surface Tuning of Band Structure. The need to tune the optical and electronic properties of graphene for applications has created a large number of proposed methods to engineer its band structure by introducing defects and/or dopants.^{203–205} Both p-doping and n-doping of graphene have been reported, the latter by doping with nitrogen species^{204,206,207} and the former by functionalization of graphene with hydrogen, oxygen, hydroxyl groups, or carboxylic groups.²⁰⁸ However,

adsorbed molecules have been found to have an extremely high mobility and low adhesion in ambient atmosphere,²⁰⁹ which makes reliable device fabrication challenging. Chemisorbed molecules change the band structure dramatically from a near-zero gap semimetal to a wide gap semiconductor, turning graphene into a highly effective insulator.^{210,211} The carrier mobility has also been shown to be decreased by more than 3 orders of magnitude to ~ 10 cm²/V·s. Overall, tuning the electronic and carrier properties of graphene in a useful range has been a very challenging task, stimulating the search for alternative 2D semiconductors with better tunability.

Even though the graphene-like band structure of silicene and germanane and the explanation for puckered *versus* flat 2D sheets was reported many years ago,²¹² much less effort has been spent in examining the tunability of these alternative elemental 2D materials, which have been successfully synthesized recently.^{15,17,18,53,211} Traditional density functional theory (DFT) suggests that a 2.75 eV direct band gap is formed after complete hydrogenation of silicene,^{213–218} whereas other types of functional groups (F, Cl, Br, and I) lead to different band gap values.²¹⁹ H-terminated Ge graphane analogues have been calculated to also have a direct band gap of 1.7 eV.²²⁰ Here we summarize recent theoretical results that explain how to controllably manipulate the relative band energies and local extrema of a covalently modifiable group IV silicon graphane analogue by termination with different organic substituents.

To develop the relationship between the band structure and the terminating functional group on silicene, Restrepo *et al.*²²¹ used DFT calculations with spin–orbit coupling and a hybrid HSE06 exchange–correlation functional,^{222,223} which features exact exchange not included in previous calculations. Silicene (H-terminated silicene) is found to have an indirect band gap of 2.94 eV with the conduction band minimum at the M point and a direct gap of 3.14 eV at the Γ point (Figure 11). The local conduction band minimum at Γ originates from the Si–H σ^* -bonds, whereas the global minimum at M corresponds to the Si–Si σ^* -bonds.²²¹ These two conduction band minima react differently to manipulation of the silicene atomic structure. Strain that increases the Si–Si bond lengths lowers the minimum at Γ while having a nearly negligible effect on the minimum at M. This leads to a change from indirect to direct band gap when the ground-state Si–Si bond length of 2.36 Å is increased to 2.40 Å. This change also causes the effective mass at the conduction band minimum to decrease from 0.18 to 0.087 m_e (48%). Changes in the Si–H bond length also mostly affect the Γ and not the M point states but are smaller than those induced by varying the Si–Si bond length. This high sensitivity of the Γ point minimum to changes in the bond between the Si atoms

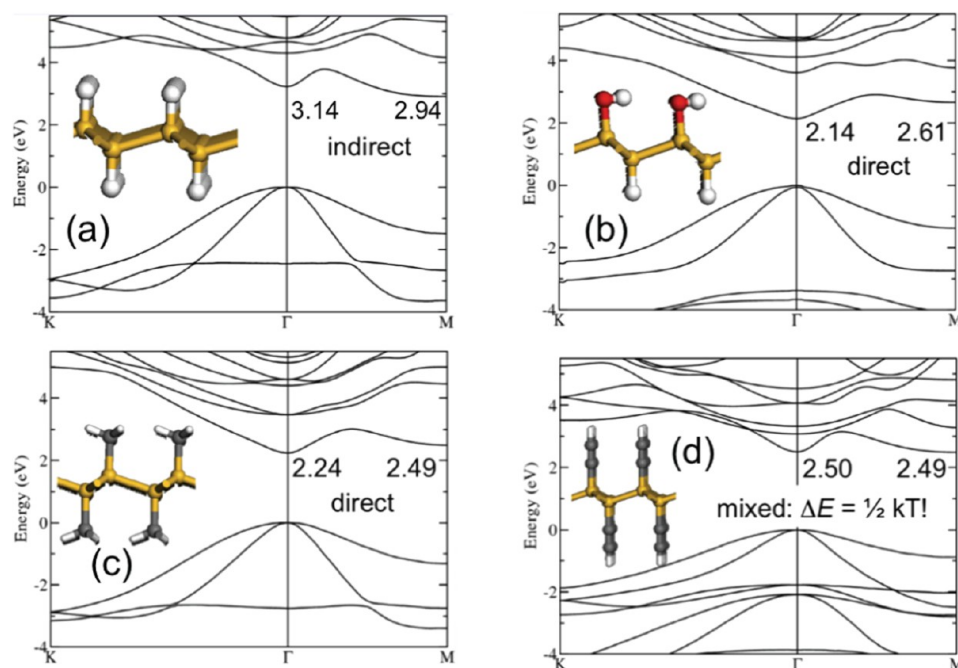


Figure 11. DFT results calculated with HSE06 hybrid potentials for silicene functionalized with (a) H, (b) half H and half hydroxyl (OH), (c) methane CH_3 , and (d) acetylene C_2H .²²¹

and the terminating hydrogen atom suggests that it is possible to tune the band gap using different terminating substituents. Small organic moieties such as methyl or ethynyl groups have also been calculated to decrease the conduction band energies and result in direct band gaps or equal conduction band minimum energies at M and Γ (Figure 11), with varying effective masses.²²¹ These results show that in contrast to graphene, where functionalization leads to drastic changes in the semimetallic band structure, silicene functionalization should allow for a wide continuous tunability in band and conduction properties and offer exciting prospects for the engineering of new electronic materials.

Two-Dimensional Materials for Spin- and Valley-tronics. Expanding charge-based microelectronics to take advantage of the spin and “valley” degrees of freedom is expected to increase computing power, reduce energy consumption, and enable the development of entirely novel devices.²²⁴ Graphene is an attractive material for spintronic applications because of its tunable carrier concentration and intrinsically low spin–orbit interaction and hyperfine couplings, which are expected to lead to long spin lifetimes.²²⁵ Here, graphene serves as an important test case for the expansion of spintronics to other 2D materials beyond graphene.

Many benchmarks toward spin functional graphene devices have already been met, the most important of which is the demonstration of room-temperature gate-tunable spin transport, as shown in Figure 12a.^{226,227} These experiments used lateral spin valves (Figure 12a, inset), which have ferromagnetic electrodes to preferentially inject spin-up or spin-down

electrons. The spin diffuses from the injection site and can be detected nonlocally by an electrode outside of the current path. Record spin lifetimes in graphene of 6.2 ns²²⁸ at 20 K have been observed (Figure 12b). Essential to this achievement was overcoming the so-called conductance mismatch problem at the injection interface with the incorporation of a high-quality, half-monolayer tunnel barrier of MgO.²²⁹ Despite these successes, measured spin lifetimes in graphene are orders of magnitude lower than those expected from *ab initio* calculations.²³⁰ A central challenge in graphene spin-transport studies is to find the source of this additional spin scattering. Recent measurements of spin transport in bilayer graphene spin valves as well as those in single-layer graphene spin valves doped with adatoms indicate that local inhomogeneities in the electronic environment are primarily responsible for the low measured spin lifetimes. If true, then while unfortunate for applications requiring robust spin coherence this extreme sensitivity of spin transport to adsorbates and screening might be intentionally exploited for novel functionality.

The spin properties of graphene provide a framework for the exploration of spin functionality in other 2D materials. MoS_2 is a specific example of how that functionality can be expanded. MoS_2 exhibits strong spin–orbit coupling, which can significantly suppress spin scattering for a certain spin direction (Figure 12c).²³¹ Though similar to graphene in other ways, the strong spin coupling in MoS_2 makes this material insensitive to spin scattering where graphene is sensitive. Achieving tunable spin scattering through creative combination of graphene and MoS_2 could provide a spectrum of new

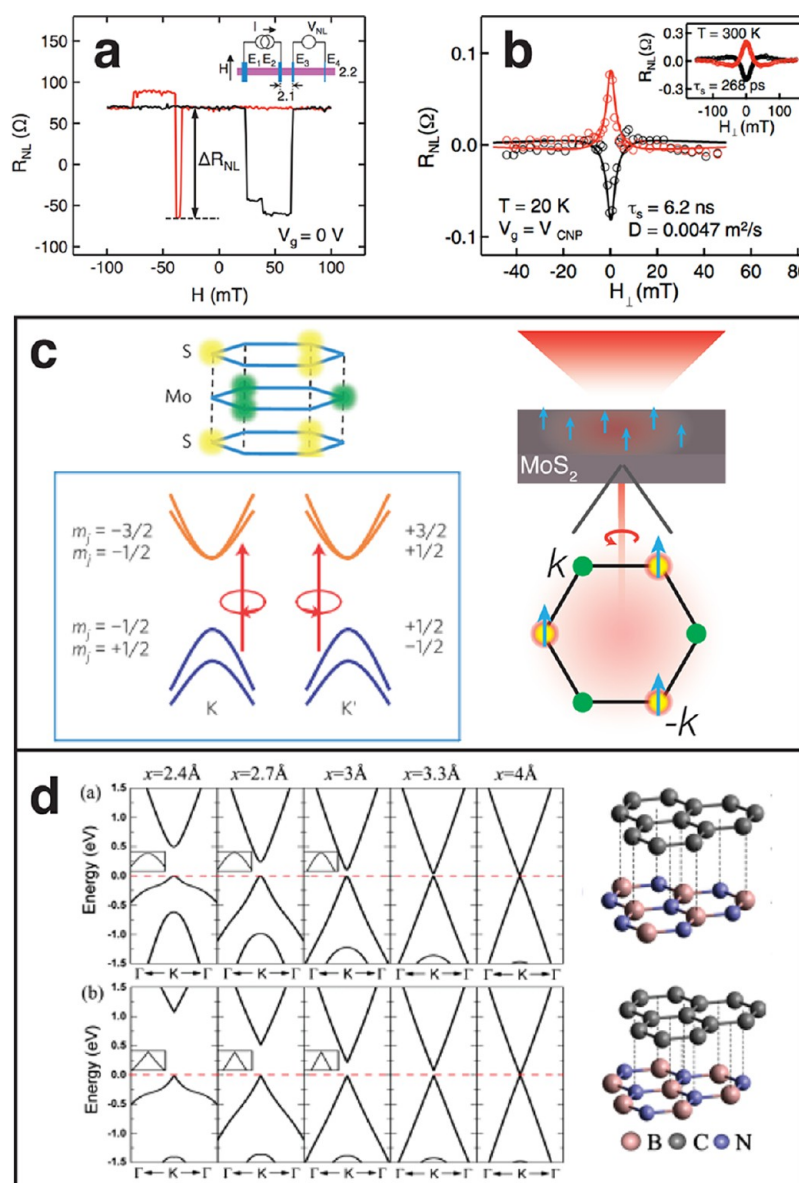


Figure 12. (a) Nonlocal magnetoresistance scans of single-layer graphene spin valves measured at room temperature. The black (red) curve shows the nonlocal resistance as the in-plane magnetic field is swept up (down). The nonlocal MR (ΔR_{NL}) of 130 Ω is indicated by the arrow. Inset: Nonlocal spin transport measurement on this device with a spacing of $L = 2.1 \mu\text{m}$ and SLG width of $W = 2.2 \mu\text{m}$.²²⁹ (b) Hanle magnetoresistance measurement (with field applied out-of-plane) of a bilayer graphene spin valve at the charge neutrality point gate voltage measured at a temperature of 20 K (inset at 300 K). The spin lifetime ($\tau_s = 6.2 \text{ ns}$) and diffusion constant ($D = 0.0047 \text{ m}^2/\text{s}$) are determined by a fit to the Hanle curve.²²⁸ (c) (Left, top) Representation of the trigonal prismatic structure of monolayer MoS_2 where each layer is a honeycomb lattice structure with each sublattice occupied by a Mo and two S atoms. (Left, bottom) The lowest-energy conduction bands and the highest-energy valence bands labeled by the z-component of their total angular momentum near the K and K' point of the Brillouin zone. The spin degeneracy at the valence band edges is lifted by spin–orbit interactions. The valley and spin degrees of freedom are coupled. Under left-circularly polarized excitation, only the K-valley is populated, whereas under right-circularly polarized excitation, only the K'-valley is populated.¹⁵⁶ (Right) Illustration of polarized spins (blue arrows) excited by right-circularly polarized light (red beam) populating the K'-valley in an MoS_2 sample. (d) Band lines near the Fermi level of BN/graphene heterobilayers with specific stacking patterns (shown on the right), calculated using local density approximation functional. The interlayer distances are $x = 5, 3.3, 3, 2.7$, and 2.4 \AA and the Fermi level is set to 0.²⁴⁰ Panel d reprinted with permission from ref 233. Copyright 2011 American Institute of Physics.

spin functionality. Even more, MoS_2 has the potential to link spin and orbital degrees of freedom, combining two of the most exciting new ideas for novel approaches to electronics: spintronics and valley-tronics.

Valley-tronics, as described above, is the manipulation of the population of degenerate low-energy

valleys that are exhibited in the band structure of some materials, including graphene and MoS_2 . Of particular relevance for electronic transport, these valleys are separated widely enough in momentum space that intervalley scattering is strongly suppressed.^{231,232} The potential for computing with valley-tronics was first

discussed for 2D electron gas devices, like AlAs and Si,²³³ but may be better realized with 2D materials with appropriate band structures. Because inversion symmetry is broken in MoS₂, the valley and spin degrees of freedom are coupled and new optical selection rules enable excitation of specific spin carriers into a specific valley, as illustrated in Figure 12c.^{156,231} This spin-valley coupling forbids independent spin or valley flipping, ensuring robust indices useful for spintronic and valleytronic applications. There is likely a lot of functionality yet to be discovered in 2D materials beyond graphene. Not only in MoS₂, just one of many transition metal dichalcogenides,¹⁴⁸ but similar phenomena may also be exploited in non-MX₂ materials such as silicene or germanane.

Finally, mechanically assembled heterostructures of van der Waals bonded 2D materials might be expected to show combined functionality of the individual layers.²³⁴ The unique properties of the independent layers, which could include spin or charge density waves, superconductivity, and carefully chosen band structures, coupled with an anticipated high rate of electron tunneling between layers could lead to emergent properties.²³⁵ Not being limited by epitaxy, like traditional thin film heterostructures, a nearly infinite number of 2D material heterostructures with various properties can be imagined. Historically, heterostructures such as semiconductor superlattices have led to the development of novel technologies such as dielectric mirrors,²³⁶ microwave metamaterials,²³⁷ and negative refraction index materials.²³⁸

Emergent functionality in 2D material heterostructures is anticipated theoretically. Density functional theory calculations predicted a band gap in graphene/BN bilayers.²³⁹ More recently, first principles calculations show that the band gap and effective electron mass in graphene/BN heterostructures might be tuned by the interlayer spacing and stacking arrangement of the individual layers, as shown in Figure 12d.²⁴⁰ Experimentally, graphene/BN heterostructures have proved important for achieving high electron mobility in graphene since the underlying BN lattice creates a better dielectric environment and reducing sensitivity to charged point defects in the underlying SiO₂.^{241,242} These heterostructures have also led to an understanding of the observed “minimal conductivity” in graphene,²⁴³ which results from charge puddles created by the nearby SiO₂ substrate.^{244,245} Additionally, tunneling field-effect transistors made from graphene/BN or graphene/MoS₂ heterostructures have been demonstrated to have high on/off ratios (up to 10 000).¹⁷¹ While these heterostructures do not yet show emergent phenomena, they represent important technological advances.

Topological Insulators. On the surface of bulk materials, either dangling bonds or band bending by an electrostatic potential can result in the appearance of

2D electronic states. Topological insulators (TIs) have unusual bulk properties that allow them to accommodate 2D electronic states on their surface.²⁴⁶ In TIs, strong spin–orbit effects create metallic electronic states on the materials' surfaces, while the bulk of the material remains insulating. Furthermore, the surface bands of TIs have an interesting electronic property in which the spin of a surface electron is always perpendicular to its momentum.²⁴⁷ This extraordinary spin property does not allow electrons to be backscattered by impurities,²⁴⁸ suggesting electronic channels of high mobility.

Following the first observation of this surface band from a Bi–Sb alloy,²⁴⁹ many materials, especially layered van der Waals materials, have been reported to be topological insulators. Layered binary chalcogenides, such as Bi₂Se₃, Bi₂Te₃, and Sb₂Te₃, are particularly interesting candidates for applications²⁵⁰ due to their relatively large bulk band gap (~0.2 eV) and simple band structure, which is similar to the Dirac band of graphene (Figure 13a,b). The existence of surface states in this family of materials is confirmed experimentally^{251–254} (Figure 13c). However, the surface electron transport is not yet straightforward to observe mainly due to the large contribution of bulk electrons. Imperfections in the bulk crystal structure create vast amounts of additional electrons, overwhelming the surface electron transport.^{253,254} Therefore, the TIs need to be engineered to reduce the bulk contribution in order to achieve transport dominated by surface electrons.

Lowering the dimensionality of these TIs might provide a route to study their surface state. Reducing sample size can suppress bulk carriers by increasing a surface-to-volume ratio.²⁵⁴ Also, low-dimensional TIs will allow the electron chemical potential to be modulated by an electric field, which can also reduce bulk carriers. TI nanodevices can be prepared from CVD-grown nanostructures^{254–256} (Figure 13d,e) and *via* the mechanical exfoliation of single crystals (Figure 13f).²⁵⁷ Field-effect measurements have successfully demonstrated the modulation of the carrier types by gate voltage, showing a potential for electronic applications.^{255–257} To control bulk electrons in TIs, compensational doping^{253,255,256} and proper surface encapsulation²⁵⁶ are crucial.

The unusual properties of the TI surface states suggest many applications not feasible in conventional materials. The intrinsic spin properties of TIs are attractive for spintronics applications.²⁵⁸ Also, superconducting TIs are expected to generate exotic quantum modes, potentially useful for quantum computation.^{258,259} Additionally the surface states can play a role in energy science by enhancing thermoelectric effects in Bi₂Te₃ and Bi₂Se₃, which are well-known thermoelectric materials.²⁶⁰ Finally, this newly discovered electronic state, often called “graphene with a

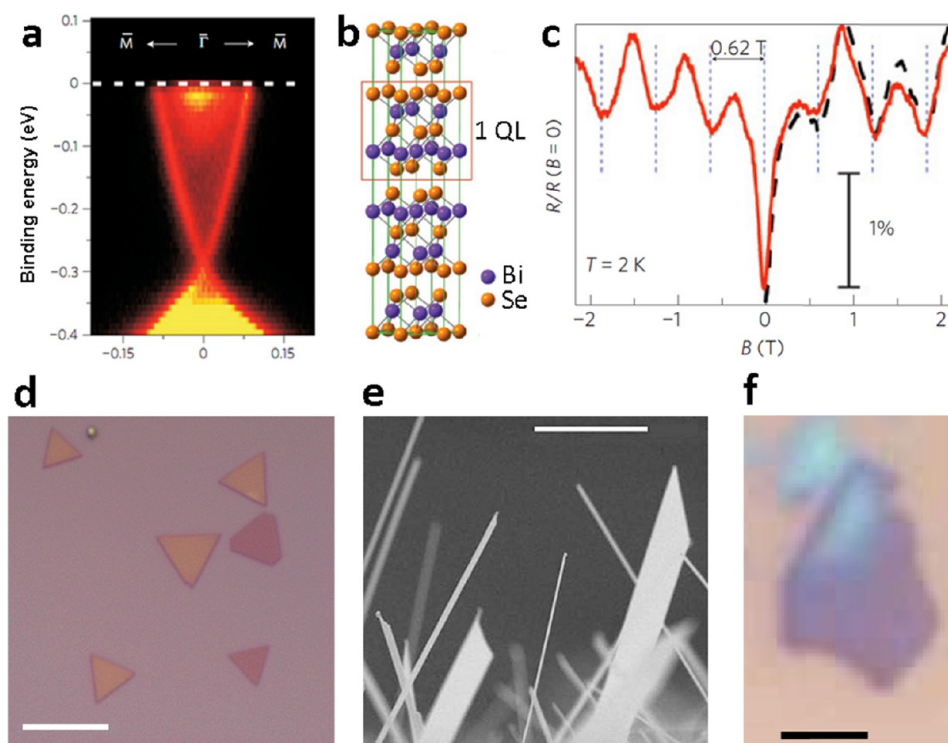


Figure 13. (a) Electronic structure of Bi_2Se_3 reconstructed by angle-resolved photoemission spectroscopy (ARPES), showing bulk conduction band (upper pocket), bulk valence band (lower pocket), and surface-state band (linear band).²⁵¹ Reprinted with permission from ref 251. Copyright 2009 Nature Publishing Group. (b) Crystal structure of Bi_2Se_3 (layered structure). Each quintuple layer is made of five atomic layers of bismuth (Bi) and selenium (Se).²⁵⁴ (c) Magnetoresistance of a Bi_2Se_3 nanoribbon in parallel magnetic field, showing periodic oscillations from the Aharonov–Bohm interference of the surface electrons.²⁵⁴ (d) Optical microscopy image of topological insulator ($\text{Bi}_x\text{Sb}_{2-x}\text{Te}_3$) nanoplates (5–10 nm thickness) on SiO_2 substrate.²⁵⁵ The scale bar indicates 5 μm . (e) Scanning electron microscopy image of topological insulator (Bi_2Se_3) nanowires and nanoribbons (50–200 nm thickness).²⁵⁶ The scale bar indicates 10 μm . (f) Optical microscopy image of a topological insulator (Bi_2Se_3) flake on SiO_2 substrate from mechanical exfoliation of a bulk crystal.²⁵⁷ The scale bar indicates 2 μm . Reprinted with permission from ref 257. Copyright 2011 Nature Publishing Group.

spin texture”, is a platform for a number of interesting studies and applications.

Thermal and Thermoelectric Properties. Recent advances in the synthesis and isolation of graphene and other atomic layered materials have enabled fundamental studies of unique thermal and thermoelectric transport properties of 2D systems, as well as the potential applications of these 2D materials for thermal management and thermoelectric energy conversion. Because of the absence of interlayer phonon scattering, the thermal conductivity of an ideal 2D system, such as suspended SLG or h-BN, is expected to be higher than the basal-plane values of their three-dimensional stacks, namely, graphite and bulk h-BN. Although the results from several micro-Raman measurements^{261,262} of suspended SLG are in agreement with these theoretical predictions, other Raman measurements^{263,264} of suspended SLG samples have yielded values comparable to or lower than the basal-plane values of graphite, as shown in Figure 14. In addition, further experiments are needed to verify recent theoretical predictions that flexural phonons (out-of-plane modes) make a large contribution to the thermal conductivity in suspended few-layer graphene and h-BN.^{265,266}

In addition, both theoretical and experimental studies have found considerable reduction of the basal-plane thermal conductivity in graphene or h-BN supported on or encased in an amorphous material^{267–269} or contaminated by polymer residue,²⁷⁰ as shown in Figure 14. In particular, the interface interaction with an amorphous material has been found to decrease the basal-plane thermal conductivity with decreasing layer thickness of FLG^{268,271} or suspended few-layer h-BN with polymer residue.²⁷² This trend is opposite to that suggested for suspended FLG or h-BN.^{261,265,266} These findings indicate that the basal-plane values for high-quality graphite and h-BN bulk crystals present a practical limit in the thermal conductivity of few-layer graphene and h-BN when these 2D layered materials are used as heat spreaders in contact with a heat source and a heat sink or as nanofillers to increase the effective thermal conductivity of a composite. However, even supported SLG can possess a basal-plane thermal conductivity higher than that of copper.²⁶⁷ Moreover, further theoretical and experimental research may potentially find new approaches to increasing the basal-plane thermal conductivity of supported graphene and h-BN by choosing the right support material or tuning

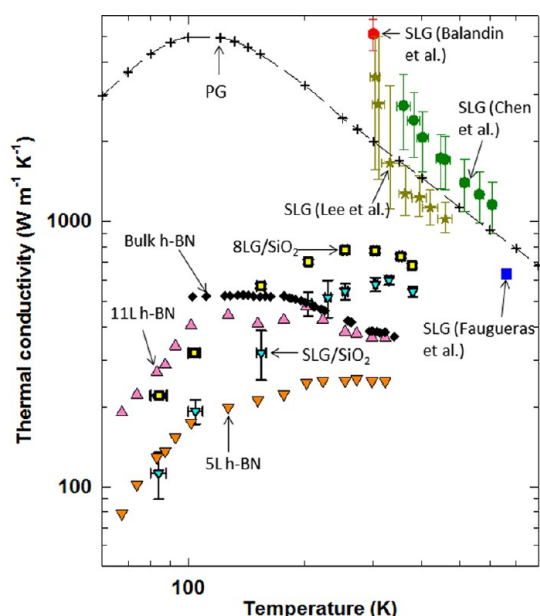


Figure 14. Comparison of reported experimental thermal conductivity values of graphite, graphene, and h-BN. The suspended SLG data are from Balandin *et al.*,³¹⁹ Chen *et al.*,²⁶² Lee *et al.*,²⁶⁴ and Faugeras *et al.*²⁶³ The data for SLG and 8-layer graphene (8LG) supported on SiO₂ are from Seol *et al.*²⁶⁷ and Sadeghi *et al.*,²⁷¹ respectively. The data for pyrolytic graphite (PG) are the recommended values by Touloukian.³²⁰ The bulk h-BN data are from Sichel *et al.*³²¹ The data for the 11- and 5-layer suspended h-BN with polymer residue are from Jo *et al.*²⁷²

the interface roughness and interaction. In particular, superior electron mobility has been found in graphene supported on h-BN compared to graphene supported on amorphous SiO₂.²⁴¹ It remains to be investigated whether graphene supported on atomically smooth h-BN may possess superior thermal transport properties compared to graphene supported on SiO₂.

The interface thermal resistance is as important in thermal transport as the basal-plane thermal conductivity of 2D layered materials. Although the cross-plane thermal conductivities of graphite and h-BN are much smaller than their basal-plane values, the cross-plane diffusive thermal resistance of few-layer graphene and h-BN is expected to be smaller than the interface thermal resistance because of the small thickness. The thermal interface resistance of graphene in contact with a dielectric or metal has been measured to be in the range of $(1-5) \times 10^{-8} \text{ K m}^2 \text{ W}^{-1}$ at room temperature.²⁷³⁻²⁷⁶ These values are not very large for the van der Waals interface, likely because graphene is rather conformal to the surface roughness.²⁷⁷ In addition, interface phonon transport between highly anisotropic graphene and a dissimilar material remains an interesting subject for theoretical study.²⁷⁸

Compared to graphene that is a semimetal, h-BN is an insulator, which can be advantageous for its applications as a heat spreader in direct contact with high-power density semiconductor nanodevices. Moreover, other 2D layered materials such as MoS₂,¹³³

silicene,⁵³ and germanane provide different band gap values suitable for various functional devices. In these functional devices made of 2D layered materials, local heating can become an important issue similar to the challenge faced by silicon nanoelectronic devices, especially if the in-plane thermal conductivity of these 2D materials is suppressed by phonon scattering by interface disorder or interactions with another material. However, little is currently known about the thermal transport properties of these 2D materials and heterostructure devices¹⁷¹ made of multiple 2D materials.

The possibly suppressed thermal conductivity (κ) of 2D layered materials with surface disorder or perturbation is desirable for thermoelectric materials. During the past two decades, nanostructures have been actively investigated for suppressing the phonon contribution to the thermal conductivity of thermoelectric materials.²⁷⁹ In such efforts, it is critical to control the interface charge states and scattering in the nanostructured materials, so that these effects do not result in a considerable reduction of the charge mobility, power factor, $S^2\sigma$, and figure of merit, $Z = S^2\sigma/\kappa$, where S is the Seebeck coefficient and σ is the electrical conductivity.²⁸⁰ Moreover, research along this direction was initially stimulated by theoretical predictions of power factor enhancement in 2D and one-dimensional quantum structures.^{281,282} Recent theoretical studies have further suggested that the power factor can be enhanced by the coupling of the two topological surface states in few quintuple layers of Bi₂Te₃ and Bi₂Se₃.²⁸³ A careful control of the surface quality and surface band bending will be required for these effects due to quantum confinement and topological surface states to be verified in experiments. These challenges suggest abundant opportunities for research in thermal and thermoelectric properties of 2D materials beyond graphene.

Applications to Transistor Scalability. Progress in the semiconductor industry has been driven by a continuous reduction of the transistor geometry. Current silicon-based field-effect transistors (FETs) feature 22 nm gate lengths, and further size reductions motivate the need to search for alternative device concepts and materials. A conventional FET consists of a semiconducting channel that is connected to source and drain electrodes and can be switched on and off by the application of a field *via* a gate electrode that is separated by a dielectric material (Figure 15a). Desirable features of switching transistors include high on/off current ratios, low power consumption, and fast switching times.

Two-dimensional materials have an innate advantage over bulk materials, like Si, for device scalability because of their favorable electrostatic properties. In particular, due to their dimensionality, these materials can approach the ideal *effective screening length*, λ , and can be operated beyond the *quantum capacitance*

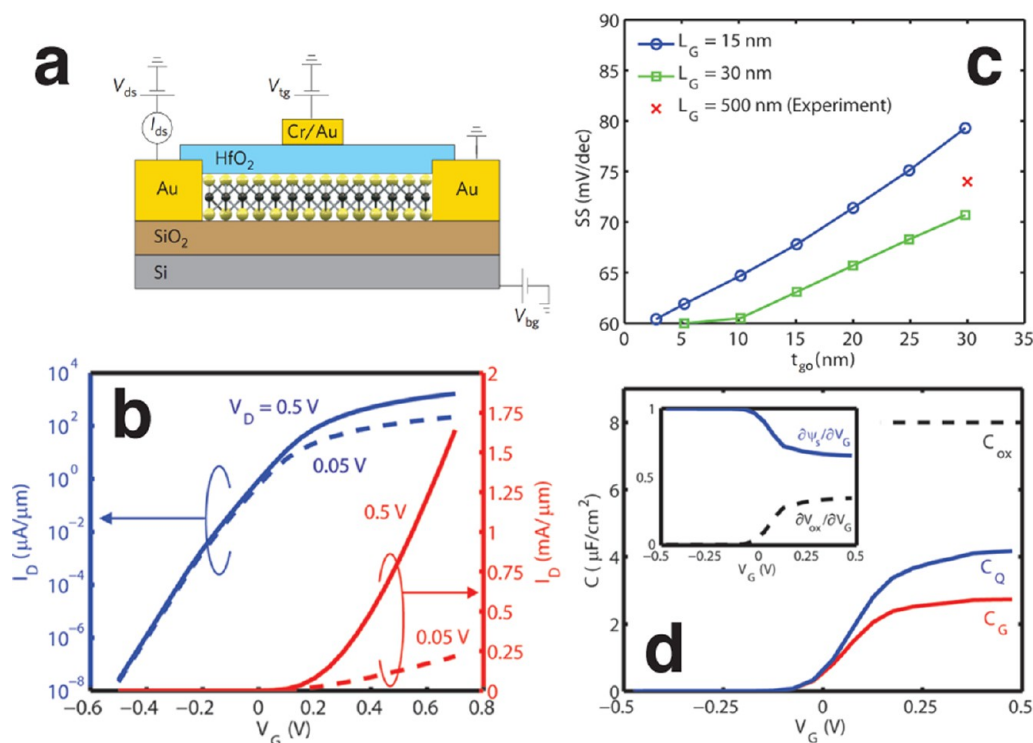


Figure 15. (a) Schematic illustration of cross section of MoS₂ FET.¹⁶³ Reprinted with permission from ref 163. Copyright 2011 Nature Publishing Group. (b) Transfer characteristic of a monolayer MoS₂ transistor in both log and linear scales. (c) Subthreshold swing as a function of gate oxide thickness for two different gate lengths. (d) Capacitance vs voltage characteristics. Inset shows the change in surface potential ψ_s with gate voltage V_G .¹⁶⁴

limit (QCL). To reduce the channel length in today's typical silicon-on-insulator transistor, the semiconductor thickness must also be reduced to ensure that 2D electrostatic screening effects are minimized.²⁸⁴ Electrostatic potential variations along the channel are screened out within a material-dependent λ .^{285,286} To prevent the electric field of the drain from being totally screened in a small channel, like those of ultrascaled MOSFETs, it is desirable for λ to be as small as possible. While the exact form of λ depends on the details of the device structure, for single and double gate geometries, it can be approximated by²⁸⁵

$$\lambda = \sqrt{\frac{\epsilon_s d_s d_{ox}}{\epsilon_{ox}}} \quad (1)$$

Here, ϵ_s and d_s denote the dielectric constant and thickness of the semiconductor, respectively, and ϵ_{ox} and d_{ox} are the respective quantities for the dielectric oxide. In either case, minimizing d_s will minimize λ . Thus, single-layer-thick 2D materials represent the best possible scenario that nature has to offer.

A second advantage of 2D material-based transistors is their ability to operate beyond the QCL, the limit at which the oxide capacitance is equal to the quantum capacitance, the capacitance due to gate-voltage-induced free charges in the channel.^{287,288} In the QCL regime, the intrinsic gate delay is reduced (τ), and the $P \cdot \tau$ (where P is the dynamic power) now decreases linearly with channel

length in the QCL regime.^{289,290} Thus the energy consumption required for switching is minimized in the QCL. In addition, many 2D materials from the dichalcogenide family, and even silicene and germanene, possess a larger band gap than bulk Si. This property could result in a much lower direct source-to-drain leakage current, which is especially important for ultrascaled transistors.²⁹¹

Recognizing the potential impact of 2D materials for transistor applications, a significant amount of work has been devoted to making these transistors in the past few years.^{163,167,292–296} Recently, the performance of MoS₂ transistors has been theoretically examined¹⁶⁴ using real space, self-consistent, and fully parallel non-equilibrium Green's function transport simulation within a $k \cdot p$ approach and band structure fitted to first principles calculations. Figure 15b shows the drain current (I_D) versus gate voltage (V_G) characteristic for a simulated MoS₂ transistor. The maximum ON current can be as high as 2 mA/μm, and the OFF current could be as small as 10 fA/μm, thereby giving an incredibly large ON/OFF ratio ($\sim 10^{10}$). Figure 15c shows the subthreshold swing as a function of gate oxide thickness. These simulation results show fantastic immunity to short channel effects. Note that almost an ideal subthreshold swing (60 mV/decade) is achievable with a reasonably large gate oxide thickness of around 5 nm even for a 30 nm channel length device. This result can be attributed to the fact that the screening length λ is very small as expected for a 2D material. Figure 15d

shows the capacitance–voltage characteristic. Note that the total capacitance (shown in blue) is much smaller than the oxide capacitance (black dashed line) and closer to the quantum capacitance (shown in solid red). This means that the device is working close to the QCL. These simulations confirm the fantastic electrostatic control, QCL operation, and low leakage current for a 2D material.

Multilayer Assemblies and Their Applications. Nanosheets (Figure 5), referring to “restacked” or assembled 2D materials, provide new opportunities and advantages for devices. For many applications, these nanosheets and their composites have inherent and predicted advantages: they can be solution processed, they can display new behavior due to their extremely high surface area, and as free-standing multilayer assemblies, they are flexible^{119,297–299} and can be manipulated either mechanically or by deposition on templates. Mixing of nanosheets with other materials, including metal nanoparticles, polymers, and small molecules, can be a route to interesting solution-phase nanocomposite hybrids, such as superlattice-like assemblies.^{99–101}

Reassembly of nanosheets into multilayer films can lead to improved properties in the areas of supercapacitors,³⁰⁰ pseudocapacitors,³⁰¹ photoconductive materials,^{302,303} and heterojunction photodiodes³⁰⁴ as new magnetic materials³⁰⁵ and as magneto-optical components.^{306,307} Additional applications include the following:

Batteries: The morphological and size advantages of nanosheets have shown improved performance as battery electrodes. For example, reassembled octatitanate nanosheets have better reversible capacities than electrodes made from bulk octatitanate, presumably due to the ability of these nanosheets to better withstand damage caused by lithium insertion and extraction.^{300,308}

Magnetic Properties: Ferromagnetic nanosheets can display unique properties such as anisotropic magnetization and stronger influences from surface atoms.³⁰⁹ For instance, gigantic magneto-optical effects have been observed in $\text{Ti}_{0.8}\text{Co}_{0.2}\text{O}_2$ nanosheets. Because these nanosheets are composed entirely of surface atoms, surface cobalt spins and their local ferromagnetic couplings are much stronger than those that occur in dilute magnetic semiconductors and bulk magnets.³⁰⁹

Photoconductors: Restacked nanosheets have higher surface area than their bulk precursors, and this aspect, coupled with the finite thickness effects on electronic structure, the reactivity, and the open framework, can lead to enhancements in nanosheet photoactivity in solar energy conversion¹¹¹ and in capacitance.³⁰¹ Furthermore, it has been recently demonstrated that a vertically oriented 2D organic/inorganic lamellar photodetector architecture can have better detectivities than sensitized nanoparticle thin films.³¹⁰ This is because the excellent 2D conduction channel allows for reduced majority carrier transit

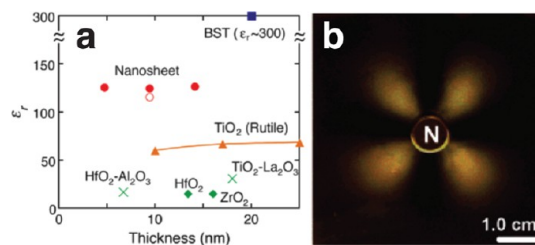


Figure 16. (a) High- k properties of titania nanosheet assemblies compared to conventional thin films. The values for the multilayered titania nanosheets are larger than what has been reported for any other high- k material.³¹² Reprinted with permission from ref 312. Copyright 2006 John Wiley and Sons. (b) Optical micrograph of a liquid crystal made from Fe_3O_4 – $\text{Ca}_2\text{Nb}_3\text{O}_{10}$ nanosheets in pyridine under an inhomogeneous magnetic field.³¹³

times, and the atomic-scale thickness of the 2D material enables a high sensitization ratio.

High Dielectric Constant Materials: As high- k dielectrics, nanosheets can be used where thin films from vapor deposition cannot. Metal oxide thin films grown by conventional vapor deposition techniques often show decreasing dielectric constants with decreasing film thickness.^{118,311,312} One reason for the degradation in dielectric properties is the high temperatures that complex vapor processing requires, often above 600 °C, which reduces the polarizability due to nonstoichiometry.³¹² Free-standing and stacks of nanosheets, however, have been shown to have low leakage current densities and high dielectric constants for thicknesses down to 10 nm (Figure 16a).^{117,118,312} Reassembled nanosheets also have the advantage of electronic isolation of each nanosheet in these multilayer assemblies.³⁰⁹

Liquid Crystals: Inorganic magnetic nanoparticles of magnetite have been mixed with niobate nanosheets and placed in a magnetic field to guide the nanoparticles' orientation.^{111,313} Light scattering shows orientational dependence on the magnetic field (Figure 16b). Potassium niobate nanosheets have been successfully functionalized with silane and dispersed in organic solvents to create liquid crystals.³¹⁴ The nanosheet colloids were dispersed in chloroform and exhibited birefringence characteristics of a nematic phase.^{111,314} Liquid-crystal properties of nanosheets have also been reported for nanosheets made of niobates³¹⁵ and $\text{KCa}_2\text{Nb}_3\text{O}_{10}$,³¹⁶ among others. The lateral dimensions, aspect ratio, and colloid concentration of the nanosheets strongly dictate the liquid-crystal properties.³¹⁵

OPPORTUNITIES AND OUTLOOK

In this nascent field of 2D materials, the salient differences between bulk and few or single layers are just starting to be understood. New fundamental studies can address single-layer scale differences in many-body interactions; phonon transport, such as flexural phonon modes; interfacial electron–electron, electron–phonon, electron–magnon, etc. coupling; excitonic and other quasiparticle properties; the nature

and impact of defects and the substrate; the influence of high doping, strain effects, and electric fields; mechanical properties; quantum size effects; and edge effects in transport. At the single-layer scale, interactions with the surroundings often dominate experimental observations, and consequently, there are a multitude of unexpected experimental challenges in isolating the intrinsic material properties. There are numerous exciting opportunities in developing the growth of high-quality large-area materials with controllable layer thicknesses. Such systems would not only expand our understanding of the underlying physics but potentially lead to the discovery of unanticipated phenomena and applications. Already, new understanding of the 2D materials has contributed to entirely new scientific frontiers such as spin- and valley-tronics. The ability to harness such unique properties and phenomena will surely lead to exciting technological advances.

Conflict of Interest: The authors declare no competing financial interest.

Acknowledgment. The topics mentioned here were discussed at a workshop entitled "2D Materials beyond Graphene" held at the Ohio State University in August 2012 and sponsored by the Army Research Office (under Award Number W911NF-12-1-0226) and the Institute for Materials Research at The Ohio State University. J.E.G. additionally wishes to acknowledge Steve Ringel and Chakrapani Varanasi for conceptual and logistical support. J.E.G. also wishes to acknowledge support from the Army Research Office (W911-NF-12-1-0481) and National Science Foundation (DMR 1201953). In the preparation of this review, we highlight a recently published review focused on the electronics of single-layer metal dichalcogenides.¹⁴⁸

REFERENCES AND NOTES

- Wilson, J. A.; Yoffe, A. D. Transition Metal Dichalcogenides Discussion and Interpretation of Observed Optical, Electrical, and Structural Properties. *Adv. Phys.* **1969**, *18*, 193–335.
- Bednorz, J. G.; Muller, K. A. Possible High- T_c Superconductivity in the Ba-La-Cu-O System. *Z. Phys. B* **1986**, *64*, 189–193.
- Kamihara, Y.; Hiramatsu, H.; Hirano, M.; Kawamura, R.; Yanagi, H.; Kamiya, T.; Hosono, H. Iron-Based Layered Superconductor: LaOFeP. *J. Am. Chem. Soc.* **2006**, *128*, 10012–10013.
- May, J. W. Platinum Surface LEED Rings. *Surf. Sci.* **1969**, *17*, 267–270.
- Novoselov, K. S.; Geim, A. K.; Morozov, S. V.; Jiang, D.; Zhang, Y.; Dubonos, S. V.; Grigorieva, I. V.; Firsov, A. A. Electric Field Effect in Atomically Thin Carbon Films. *Science* **2004**, *306*, 666–669.
- Stankovich, S.; Dikin, D. A.; Dommett, G. H. B.; Kohlhaas, K. M.; Zimney, E. J.; Stach, E. A.; Piner, R. D.; Nguyen, S. T.; Ruoff, R. S. Graphene-Based Composite Materials. *Nature* **2006**, *442*, 282–286.
- Kim, K. S.; Zhao, Y.; Jang, H.; Lee, S. Y.; Kim, J. M.; Kim, K. S.; Ahn, J.-H.; Kim, P.; Choi, J.-Y.; Hong, B. H. Large-Scale Pattern Growth of Graphene Films for Stretchable Transparent Electrodes. *Nature* **2009**, *457*, 706–710.
- Yang, H.; Heo, J.; Park, S.; Song, H. J.; Seo, D. H.; Byun, K. E.; Kim, P.; Yoo, I.; Chung, H. J.; Kim, K. Graphene Barristor, a Triode Device with a Gate-Controlled Schottky Barrier. *Science* **2012**, *336*, 1140–1143.
- Frindt, R. F. Single Crystals of MoS₂ Several Molecular Layers Thick. *J. Appl. Phys.* **1966**, *37*, 1928–1929.
- Joensen, P.; Frindt, R. F.; Morrison, S. R. Single-Layer MoS₂. *Mater. Res. Bull.* **1986**, *21*, 457–461.
- Frindt, R. F. Superconductivity in Ultrathin NbSe₂ Layers. *Phys. Rev. Lett.* **1972**, *28*, 299–301.
- Divigalpitiya, W. M. R.; Frindt, R. F.; Morrison, S. R. Inclusion Systems of Organic-Molecules in Restacked Single-Layer Molybdenum Disulfide. *Science* **1989**, *246*, 369–371.
- Yang, D.; Sandoval, S. J.; Divigalpitiya, W. M. R.; Irwin, J. C.; Frindt, R. F. Structure of Single-Molecular-Layer MoS₂. *Phys. Rev. B* **1991**, *43*, 12053–12056.
- Aufrey, B.; Kara, A.; Vizzini, S.; Oughaddou, H.; Leandri, C.; Ealet, B.; Le Lay, G. Graphene-like Silicon Nanoribbons on Ag(110): A Possible Formation of Silicene. *Appl. Phys. Lett.* **2010**, *96*, 183102.
- Lalmi, B.; Oughaddou, H.; Enriquez, H.; Kara, A.; Vizzini, S.; Ealet, B.; Aufray, B. Epitaxial Growth of a Silicene Sheet. *Appl. Phys. Lett.* **2010**, *97*, 223109.
- Kara, A.; Enriquez, H.; Seitsonen, A. P.; Voon, L.; Vizzini, S.; Aufray, B.; Oughaddou, H. A Review on Silicene—New Candidate for Electronics. *Surf. Sci. Rep.* **2012**, *67*, 1–18.
- Flurence, A.; Friedlein, R.; Ozaki, T.; Kawai, H.; Wang, Y.; Yamada-Takamura, Y. Experimental Evidence for Epitaxial Silicene on Diboride Thin Films. *Phys. Rev. Lett.* **2012**, *108*, 245501.
- Bianco, E.; Butler, S.; Jiang, S.; Restrepo, O. D.; Windl, W.; Goldberger, J. E. Stability and Exfoliation of Germanane; a Germanium Graphene Analogue. *ACS Nano* **2013**, DOI: 10.1021/nn4009406.
- Consador, F.; Fife, A. A.; Frindt, R. F.; Gygas, S. Construction and Properties of Weak-Link Detectors Using Superconducting Layer Structure. *Appl. Phys. Lett.* **1971**, *18*, 233–235.
- Novoselov, K. S.; Jiang, D.; Schedin, F.; Booth, T. J.; Khotkevich, V. V.; Morozov, S. V.; Geim, A. K. Two-Dimensional Atomic Crystals. *Proc. Natl. Acad. Sci. U.S.A.* **2005**, *102*, 10451–10453.
- Shahil, K. M. F.; Hossain, M. Z.; Teweldebrhan, D.; Balandin, A. A. Crystal Symmetry Breaking in Few-Quintuple Bi₂Te₃ Films: Applications in Nanometrology of Topological Insulators. *Appl. Phys. Lett.* **2010**, *96*, 153103.
- Goli, P.; Khan, J.; Wickramaratne, D.; Lake, R. K.; Balandin, A. A. Charge Density Waves in Exfoliated Films of van der Waals Materials: Evolution of Raman Spectrum in TiSe₂. *Nano Lett.* **2012**, *12*, 5941–5945.
- Kim, K. K.; Hsu, A.; Jia, X.; Kim, S. M.; Shi, Y.; Hofmann, M.; Nezich, D.; Rodriguez-Nieva, J. F.; Dresselhaus, M.; Palacios, T.; *et al.* Synthesis of Monolayer Hexagonal Boron Nitride on Cu Foil Using Chemical Vapor Deposition. *Nano Lett.* **2012**, *12*, 161–166.
- Kong, D.; Dang, W.; Cha, J. J.; Li, H.; Meister, S.; Peng, H.; Liu, Z.; Cui, Y. Few-Layer Nanoplates of Bi₂Se₃ and Bi₂Te₃ with Highly Tunable Chemical Potential. *Nano Lett.* **2010**, *10*, 2245–2250.
- Liu, D. F.; Zhang, W. H.; Mou, D. X.; He, J. F.; Ou, Y. B.; Wang, Q. Y.; Li, Z.; Wang, L. L.; Zhao, L.; He, S. L.; *et al.* Electronic Origin of High-Temperature Superconductivity in Single-Layer FeSe Superconductor. *Nat. Commun.* **2012**, *3*, 931.
- Vogg, G.; Brandt, M. S.; Stutzmann, M. Polygermyne—A Prototype System for Layered Germanium Polymers. *Adv. Mater.* **2000**, *12*, 1278–1281.
- Vogg, G.; Meyer, A. J. P.; Miesner, C.; Brandt, M. S.; Stutzmann, M. Efficient Tunable Luminescence of SiGe Alloy Sheet Polymers. *Appl. Phys. Lett.* **2001**, *78*, 3956–3958.
- Okamoto, H.; Sugiyama, Y.; Nakano, H. Synthesis and Modification of Silicon Nanosheets and Other Silicon Nanomaterials. *Chem.—Eur. J.* **2011**, *17*, 9864–9887.
- Chernozatonskii, L. A.; Sorokin, P. B.; Kvashnin, A. G.; Kvashnin, D. G. Diamond-like C₂H Nanolayer, Diamane: Simulation of the Structure and Properties. *JETP Lett.* **2009**, *90*, 134–138.
- Chernozatonskii, L. A.; Sorokin, P. B. Nanoengineering Structures on Graphene with Adsorbed Hydrogen "Lines". *J. Phys. Chem. C* **2010**, *114*, 3225–3229.
- Chernozatonskii, L. A.; Sorokin, P. B.; Kuzubov, A. A.; Sorokin, B. P.; Kvashnin, A. G.; Kvashnin, D. G.; Avramov, P. V.; Yakobson, B. I. Influence of Size Effect on the Electronic and Elastic Properties of Diamond Films with Nanometer Thickness. *J. Phys. Chem. C* **2011**, *115*, 132–136.

32. Chernozatonskii, L. A.; Mavrin, B. N.; Sorokin, P. B. Determination of Ultrathin Diamond Films by Raman Spectroscopy. *Phys. Status Solidi B* **2012**, *249*, 1550–1554.
33. Naguib, M.; Kurtoglu, M.; Presser, V.; Lu, J.; Niu, J.; Heon, M.; Hultman, L.; Gogotsi, Y.; Barsoum, M. W. Two-Dimensional Nanocrystals Produced by Exfoliation of Ti_3AlC_2 . *Adv. Mater.* **2011**, *23*, 4248–4253.
34. Kawamura, F.; Yusa, H.; Taniguchi, T. Synthesis of Rhenium Nitride Crystals with MoS_2 Structure. *Appl. Phys. Lett.* **2012**, *100*, 251910.
35. Tulskey, E. G.; Long, J. R. Dimensional Reduction: A Practical Formalism for Manipulating Solid Structures. *Chem. Mater.* **2001**, *13*, 1149–1166.
36. Long, J. R.; McCarty, L. S.; Holm, R. H. A Solid-State Route to Molecular Clusters: Access to the Solution Chemistry of $[\text{Re}_6\text{Q}_8]^{2+}$ (Q = S, Se) Core-Containing Clusters via Dimensional Reduction. *J. Am. Chem. Soc.* **1996**, *118*, 4603–4616.
37. Kagan, C. R.; Mitzi, D. B.; Dimitrakopoulos, C. D. Organic–Inorganic Hybrid Materials as Semiconducting Channels in Thin-Film Field-Effect Transistors. *Science* **1999**, *286*, 945–947.
38. Huang, X.; Li, J.; Fu, H. The First Covalent Organic–Inorganic Networks of Hybrid Chalcogenides: Structures That May Lead to a New Type of Quantum Wells. *J. Am. Chem. Soc.* **2000**, *122*, 8789–8790.
39. Mitzi, D. B. Solution Processing of Chalcogenide Semiconductors via Dimensional Reduction. *Adv. Mater.* **2009**, *21*, 3141–3158.
40. Huang, X.; Roushan, M.; Emge, T. J.; Bi, W.; Thiagarajan, S.; Cheng, J.-H.; Yang, R.; Li, J. Flexible Hybrid Semiconductors with Low Thermal Conductivity: The Role of Organic Diamines. *Angew. Chem., Int. Ed.* **2009**, *48*, 7871–7874.
41. Sun, Y.; Sun, Z.; Gao, S.; Cheng, H.; Liu, Q.; Piao, J.; Yao, T.; Wu, C.; Hu, S.; Wei, S. Fabrication of Flexible and Free-standing Zinc Chalcogenide Single Layers. *Nat. Commun.* **2012**, *3*, 1057.
42. Schaak, R. E.; Mallouk, T. E. Prying Apart Ruddlesden-Popper Phases: Exfoliation into Sheets and Nanotubes for Assembly of Perovskite Thin Films. *Chem. Mater.* **2000**, *12*, 3427–3434.
43. Schaak, R. E.; Mallouk, T. E. Self-Assembly of Tiled Perovskite Monolayer and Multilayer Thin Films. *Chem. Mater.* **2000**, *12*, 2513–2516.
44. Schaak, R. E.; Mallouk, T. E. Topochemical Synthesis of Three-Dimensional Perovskites from Lamellar Precursors. *J. Am. Chem. Soc.* **2000**, *122*, 2798–2803.
45. Schaak, R. E.; Mallouk, T. E. Perovskites by Design: A Toolbox of Solid-State Reactions. *Chem. Mater.* **2002**, *14*, 1455–1471.
46. Schaak, R. E.; Mallouk, T. E. Exfoliation of Layered Rutile and Perovskite Tungstates. *Chem. Commun.* **2002**, 706–707.
47. Ida, S.; Ogata, C.; Eguchi, M.; Youngblood, W. J.; Mallouk, T. E.; Matsumoto, Y. Photoluminescence of Perovskite Nanosheets Prepared by Exfoliation of Layered Oxides, $\text{K}_2\text{Ln}_2\text{Ti}_3\text{O}_{10}$, KLnNb_2O_7 , and $\text{RbLnTa}_2\text{O}_7$ (Ln: Lanthanide Ion). *J. Am. Chem. Soc.* **2008**, *130*, 7052–7059.
48. Tanaka, T.; Ebina, Y.; Takada, K.; Kurashima, K.; Sasaki, T. Oversized Titania Nanosheet Crystallites Derived from Flux-Grown Layered Titanate Single Crystals. *Chem. Mater.* **2003**, *15*, 3564–3568.
49. Kim, T. W.; Oh, E. J.; Jee, A. Y.; Lim, S. T.; Park, D. H.; Lee, M.; Hyun, S. H.; Choy, J. H.; Hwang, S. J. Soft-Chemical Exfoliation Route to Layered Cobalt Oxide Monolayers and Its Application for Film Deposition and Nanoparticle Synthesis. *Chem.—Eur. J.* **2009**, *15*, 10752–10761.
50. Ida, S.; Shiga, D.; Koinuma, M.; Matsumoto, Y. Synthesis of Hexagonal Nickel Hydroxide Nanosheets by Exfoliation of Layered Nickel Hydroxide Intercalated with Dodecyl Sulfate Ions. *J. Am. Chem. Soc.* **2008**, *130*, 14038–14039.
51. Hu, L.; Ma, R.; Ozawa, T. C.; Sasaki, T. Exfoliation of Layered Europium Hydroxide into Unilamellar Nanosheets. *Chem. Asian J.* **2010**, *5*, 248–251.
52. Omomo, Y.; Sasaki, T.; Wang, L. Z.; Watanabe, M. Redoxable Nanosheet Crystallites of MnO_2 Derived via Delamination of a Layered Manganese Oxide. *J. Am. Chem. Soc.* **2003**, *125*, 3568–3575.
53. Vogt, P.; De Padova, P.; Quaresima, C.; Avila, J.; Frantzeskakis, E.; Asensio, M. C.; Resta, A.; Ealet, B.; Le Lay, G. Silicene: Compelling Experimental Evidence for Graphenelike Two-Dimensional Silicon. *Phys. Rev. Lett.* **2012**, *108*, 155501.
54. Hirjibehedin, C. F.; Lin, C. Y.; Otte, A. F.; Ternes, M.; Lutz, C. P.; Jones, B. A.; Heinrich, A. J. Large Magnetic Anisotropy of a Single Atomic Spin Embedded in a Surface Molecular Network. *Science* **2007**, *317*, 1199–1203.
55. Ruggiero, C. D.; Badal, M.; Choi, T.; Gohlke, D.; Stroud, D.; Gupta, J. A. Emergence of Surface States in Nanoscale Cu_2N Islands. *Phys. Rev. B* **2011**, *83*, 245430.
56. Heinrich, A. J.; Gupta, J. A.; Lutz, C. P.; Eigler, D. M. Single-Atom Spin-Flip Spectroscopy. *Science* **2004**, *306*, 466–469.
57. Olsson, F. E.; Paavilainen, S.; Persson, M.; Repp, J.; Meyer, G. Multiple Charge States of Ag Atoms on Ultrathin NaCl Films. *Phys. Rev. Lett.* **2007**, *98*, 176803.
58. Sterrer, M.; Risse, T.; Pozzoni, U. M.; Giordano, L.; Heyde, M.; Rust, H. P.; Pacchioni, G.; Freund, H. J. Control of the Charge State of Metal Atoms on Thin MgO Films. *Phys. Rev. Lett.* **2007**, *98*, 096107.
59. Potapenko, D. V.; Hrbek, J.; Osgood, R. M. Scanning Tunneling Microscopy Study of Titanium Oxide Nanocrystals Prepared on Au(111) by Reactive-Layer-Assisted Deposition. *ACS Nano* **2008**, *2*, 1353–1362.
60. Peng, Y. Y.; Meng, Z. Y.; Zhong, C.; Lu, J.; Yu, W. C.; Jia, Y. B.; Qian, Y. T. Hydrothermal Synthesis and Characterization of Single-Molecular-Layer MoS_2 and MoSe_2 . *Chem. Lett.* **2001**, 772–773.
61. Son, J. S.; Wen, X.-D.; Joo, J.; Chae, J.; Baek, S.-i.; Park, K.; Kim, J. H.; An, K.; Yu, J. H.; Kwon, S. G.; et al. Large-Scale Soft Colloidal Template Synthesis of 1.4 nm Thick CdSe Nanosheets. *Angew. Chem., Int. Ed.* **2009**, *48*, 6861–6864.
62. Vaughn, D. D., II; Patel, R. J.; Hickner, M. A.; Schaak, R. E. Single-Crystal Colloidal Nanosheets of GeS and GeSe. *J. Am. Chem. Soc.* **2010**, *132*, 15170–15172.
63. Schliehe, C.; Juarez, B. H.; Pelletier, M.; Jander, S.; Greshnykh, D.; Nagel, M.; Meyer, A.; Foerster, S.; Komowski, A.; Klinke, C.; et al. Ultrathin PbS Sheets by Two-Dimensional Oriented Attachment. *Science* **2010**, *329*, 550–553.
64. Feng, J.; Peng, L.; Wu, C.; Sun, X.; Hu, S.; Lin, C.; Dai, J.; Yang, J.; Xie, Y. Ultrathin Nanosheets: Giant Moisture Responsiveness of VS_2 Ultrathin Nanosheets for Novel Touchless Positioning Interface. *Adv. Mater.* **2012**, *24*, 1917–1917.
65. Jeong, S.; Yoo, D.; Jang, J.-t.; Kim, M.; Cheon, J. Well-Defined Colloidal 2-D Layered Transition-Metal Chalcogenide Nanocrystals via Generalized Synthetic Protocols. *J. Am. Chem. Soc.* **2012**, *134*, 18233–18236.
66. Plashnitsa, V. V.; Vietmeyer, F.; Petchsang, N.; Tongying, P.; Kosel, T. H.; Kuno, M. Synthetic Strategy and Structural and Optical Characterization of Thin Highly Crystalline Titanium Disulfide Nanosheets. *J. Phys. Chem. Lett.* **2012**, *3*, 1554–1558.
67. Davis, R. E.; Nakshben, H. F. Sulfur in Amine Solvents. *J. Am. Chem. Soc.* **1962**, *84*, 2085–2090.
68. Levi, T. G.; Solfuri, E. Polisolfuri Di Basi Organiche. *Gazz. Chim. Ital.* **1930**, *60*, 975–987.
69. Levi, T. G. Politioamine Superiori Alle Ditio. *Gazz. Chim. Ital.* **1931**, *61*, 286–293.
70. Thomson, J. W.; Nagashima, K.; Macdonald, P. M.; Ozin, G. A. From Sulfur-Amine Solutions to Metal Sulfide Nanocrystals: Peering into the Oleylamine-Sulfur Black Box. *J. Am. Chem. Soc.* **2011**, *133*, 5036–5041.
71. Cui, Y.; Lauhon, L. J.; Gudiksen, M. S.; Wang, J.; Lieber, C. M. Diameter-Controlled Synthesis of Single-Crystal Silicon Nanowires. *Appl. Phys. Lett.* **2001**, *78*, 2214.
72. Kong, J.; Cassell, A. M.; Dai, H. J. Chemical Vapor Deposition of Methane for Single-Walled Carbon Nanotubes. *Chem. Phys. Lett.* **1998**, *292*, 567–574.
73. Li, X.; Cai, W.; An, J.; Kim, S.; Nah, J.; Yang, D.; Piner, R.; Velamakanni, A.; Jung, I.; Tutuc, E.; et al. Large-Area Synthesis of High-Quality and Uniform Graphene Films on Copper Foils. *Science* **2009**, *324*, 1312–1314.

74. Li, C.; Huang, L.; Snigdha, G. P.; Yu, Y.; Cao, L. Role of Boundary Layer Diffusion in Vapor Deposition Growth of Chalcogenide Nanosheets: The Case of GeS. *ACS Nano* **2012**, *6*, 8868–8877.
75. Shi, Y.; Zhou, W.; Lu, A. Y.; Fang, W.; Lee, Y. H.; Hsu, A. L.; Kim, S. M.; Kim, K. K.; Yang, H. Y.; Li, L. J.; *et al.* van der Waals Epitaxy of MoS₂ Layers Using Graphene as Growth Templates. *Nano Lett.* **2012**, *12*, 2784–2791.
76. Koma, A.; Ueno, K.; Saiki, K. Heteroepitaxial Growth by van der Waals Interaction in One-Dimensional, Two-Dimensional, and Three-Dimensional Materials. *J. Cryst. Growth* **1991**, *111*, 1029–1032.
77. Koma, A. Van der Waals Epitaxy—A New Epitaxial-Growth Method for a Highly Lattice-Mismatched System. *Thin Solid Films* **1992**, *216*, 72–76.
78. Hagstrom, S.; Lyon, H. B.; Somorjai, G. A. Surface Structures on Clean Platinum (100) Surface. *Phys. Rev. Lett.* **1965**, *15*, 491–493.
79. Lyon, H. B.; Somorjai, G. A. Low-Energy Electron-Diffraction Study of Clean (100), (111), and (110) Faces of Platinum. *J. Chem. Phys.* **1967**, *46*, 2539–2550.
80. Morgan, A. E.; Somorjai, G. A. Low Energy Electron Diffraction Studies of Gas Adsorption on Platinum (100) Single Crystal Surface. *Surf. Sci.* **1968**, *12*, 405–425.
81. Eizenberg, M.; Blakely, J. M. Carbon Interaction with Nickel Surface—Monolayer Formation and Structural Stability. *J. Chem. Phys.* **1979**, *71*, 3467–3477.
82. Eizenberg, M.; Blakely, J. M. Carbon Monolayer Phase Condensation on Ni(111). *Surf. Sci.* **1979**, *82*, 228–236.
83. Sutter, P. W.; Flege, J.-I.; Sutter, E. A. Epitaxial Graphene on Ruthenium. *Nat. Mater.* **2008**, *7*, 406–411.
84. Coraux, J.; N'Diaye, A. T.; Busse, C.; Michely, T. Structural Coherency of Graphene on Ir(111). *Nano Lett.* **2008**, *8*, 565–570.
85. Hamilton, J. C.; Blakely, J. M. Carbon Segregation to Single-Crystal Surfaces of Pt, Pd and Co. *Surf. Sci.* **1980**, *91*, 199–217.
86. Ramon, M. E.; Gupta, A.; Corbet, C.; Ferrer, D. A.; Movva, H. C. P.; Carpenter, G.; Colombo, L.; Bourianoff, G.; Doczy, M.; Akinwande, D.; *et al.* CMOS-Compatible Synthesis of Large-Area, High-Mobility Graphene by Chemical Vapor Deposition of Acetylene on Cobalt Thin Films. *ACS Nano* **2011**, *5*, 7198–7204.
87. Reina, A.; Jia, X.; Ho, J.; Nezich, D.; Son, H.; Bulovic, V.; Dresselhaus, M. S.; Kong, J. Large Area, Few-Layer Graphene Films on Arbitrary Substrates by Chemical Vapor Deposition. *Nano Lett.* **2009**, *9*, 30–35.
88. Berger, C.; Song, Z. M.; Li, T. B.; Li, X. B.; Ogbazghi, A. Y.; Feng, R.; Dai, Z. T.; Marchenkov, A. N.; Conrad, E. H.; First, P. N.; *et al.* Ultrathin Epitaxial Graphite: 2D Electron Gas Properties and a Route toward Graphene-Based Nanoelectronics. *J. Phys. Chem. B* **2004**, *108*, 19912–19916.
89. Li, X.; Cai, W.; Colombo, L.; Ruoff, R. S. Evolution of Graphene Growth on Ni and Cu by Carbon Isotope Labeling. *Nano Lett.* **2009**, *9*, 4268–4272.
90. Li, X.; Magnuson, C. W.; Venugopal, A.; An, J.; Suk, J. W.; Han, B.; Borysiak, M.; Cai, W.; Velamakanni, A.; Zhu, Y.; *et al.* Graphene Films with Large Domain Size by a Two-Step Chemical Vapor Deposition Process. *Nano Lett.* **2010**, *10*, 4328–4334.
91. Li, X.; Magnuson, C. W.; Venugopal, A.; Tromp, R. M.; Hannon, J. B.; Vogel, E. M.; Colombo, L.; Ruoff, R. S. Large-Area Graphene Single Crystals Grown by Low-Pressure Chemical Vapor Deposition of Methane on Copper. *J. Am. Chem. Soc.* **2011**, *133*, 2816–2819.
92. Wang, H.; Wang, G.; Bao, P.; Yang, S.; Zhu, W.; Xie, X.; Zhang, W.-J. Controllable Synthesis of Submillimeter Single-Crystal Monolayer Graphene Domains on Copper Foils by Suppressing Nucleation. *J. Am. Chem. Soc.* **2011**, *134*, 3627–3630.
93. Yan, Z.; Lin, J.; Peng, Z.; Sun, Z.; Zhu, Y.; Li, L.; Xiang, C.; Samuel, E. L.; Kittrell, C.; Tour, J. M. Toward the Synthesis of Wafer-Scale Single-Crystal Graphene on Copper Foils. *ACS Nano* **2012**, *6*, 9110–9117.
94. Weatherup, R. S.; Dlubak, B.; Hofmann, S. Kinetic Control of Catalytic CVD for High-Quality Graphene at Low Temperatures. *ACS Nano* **2012**, *6*, 9996–10003.
95. Najmaei, S.; Liu, Z.; Zhou, W.; Zou, X.; Shi, G.; Lei, S.; Yakobson, B. I.; Idrobo, J. C.; Ajayan, P. M.; Luo, J. Vapor Phase Growth and Grain Boundary Structure of Molybdenum Disulfide Atomic Layers. *arXiv:1301.1985*, **2013**.
96. Nagashima, A.; Tejima, N.; Gamou, Y.; Kawai, T.; Oshima, C. Electronic-Structure of Monolayer Hexagonal Boron-Nitride Physisorbed on Metal-Surfaces. *Phys. Rev. Lett.* **1995**, *75*, 3918–3921.
97. Song, L.; Ci, L.; Lu, H.; Sorokin, P. B.; Jin, C.; Ni, J.; Kvashnin, A. G.; Kvashnin, D. G.; Lou, J.; Yakobson, B. I.; *et al.* Large Scale Growth and Characterization of Atomic Hexagonal Boron Nitride Layers. *Nano Lett.* **2010**, *10*, 3209–3215.
98. Ismach, A.; Chou, H.; Ferrer, D. A.; Wu, Y.; McDonnell, S.; Floresca, H. C.; Covacevich, A.; Pope, C.; Piner, R.; Kim, M. J.; *et al.* Toward the Controlled Synthesis of Hexagonal Boron Nitride Films. *ACS Nano* **2012**, *6*, 6378–6385.
99. Kim, J. Y.; Osterloh, F. E. Planar Gold Nanoparticle Clusters as Microscale Mirrors. *J. Am. Chem. Soc.* **2006**, *128*, 3868–3869.
100. Hata, H.; Kubo, S.; Kobayashi, Y.; Mallouk, T. E. Intercalation of Well-Dispersed Gold Nanoparticles into Layered Oxide Nanosheets through Intercalation of a Polyamine. *J. Am. Chem. Soc.* **2007**, *129*, 3064–3065.
101. Osada, M.; Sasaki, T. Exfoliated Oxide Nanosheets: New Solution to Nanoelectronics. *J. Mater. Chem.* **2009**, *19*, 2503–2511.
102. Keller, S. W.; Kim, H.-N.; Mallouk, T. E. Layer-by-Layer Assembly of Intercalation Compounds and Heterostructures on Surfaces: Toward Molecular “Beaker” Epitaxy. *J. Am. Chem. Soc.* **1994**, *116*, 8817–8818.
103. Kim, H.-N.; Keller, S. W.; Mallouk, T. E.; Schmitt, J.; Decher, G. Characterization of Zirconium Phosphate/Polycarbonate Thin Films Grown by Sequential Adsorption Reactions. *Chem. Mater.* **1997**, *9*, 1414–1421.
104. Fang, M.; Kim, C. H.; Saupe, G. B.; Kim, H.-N.; Waraksa, C. C.; Miwa, T.; Fujishima, A.; Mallouk, T. E. Layer-by-Layer Growth and Condensation Reactions of Niobate and Titanoniobate Thin Films. *Chem. Mater.* **1999**, *11*, 1526–1532.
105. Hoertz, P. G.; Mallouk, T. E. Light-to-Chemical Energy Conversion in Lamellar Solids and Thin Films. *Inorg. Chem.* **2005**, *44*, 6828–6840.
106. Saruwatari, K.; Sato, H.; Idei, T.; Kameda, J.; Yamagishi, A.; Takagaki, A.; Domen, K. Photoconductive Properties of Organic–Inorganic Hybrid Films of Layered Perovskite-Type Niobate. *J. Phys. Chem. B* **2005**, *109*, 12410–12416.
107. Muramatsu, M.; Akatsuka, K.; Ebina, Y.; Wang, K.; Sasaki, T.; Ishida, T.; Miyake, K.; Haga, M.-a. Fabrication of Densely Packed Titania Nanosheet Films on Solid Surface by Use of Langmuir–Blodgett Deposition Method without Amphiphilic Additives. *Langmuir* **2005**, *21*, 6590–6595.
108. Cote, L. J.; Kim, F.; Huang, J. Langmuir–Blodgett Assembly of Graphite Oxide Single Layers. *J. Am. Chem. Soc.* **2009**, *131*, 1043–1049.
109. Li, L.; Ma, R.; Ebina, Y.; Fukuda, K.; Takada, K.; Sasaki, T. Layer-by-Layer Assembly and Spontaneous Flocculation of Oppositely Charged Oxide and Hydroxide Nanosheets into Inorganic Sandwich Layered Materials. *J. Am. Chem. Soc.* **2007**, *129*, 8000–8007.
110. Unal, U.; Matsumoto, Y.; Tamoto, N.; Koinuma, M.; Machida, M.; Izawa, K. Visible Light Photoelectrochemical Activity of K₄Nb₆O₁₇ Intercalated with Photoactive Complexes by Electrostatic Self-Assembly Deposition. *J. Solid State Chem.* **2006**, *179*, 33–40.
111. Bizeto, M. A.; Shiguihara, A. L.; Constantino, V. R. L. Layered Niobate Nanosheets: Building Blocks for Advanced Materials Assembly. *J. Mater. Chem.* **2009**, *19*, 2512–2525.
112. Wang, X.; Zhi, C.; Li, L.; Zeng, H.; Li, C.; Mitome, M.; Golberg, D.; Bando, Y. “Chemical Blowing” of Thin-Walled Bubbles: High-Throughput Fabrication of Large-Area, Few-Layered

- BN and C-x-BN Nanosheets. *Adv. Mater.* **2011**, *23*, 4072–4076.
113. Wang, X.; Pakdel, A.; Zhi, C.; Watanabe, K.; Sekiguchi, T.; Golberg, D.; Bando, Y. High-Yield Boron Nitride Nanosheets from "Chemical Blowing": Towards Practical Applications in Polymer Composites. *J. Phys.: Condens. Matter* **2012**, *24*, 314205–314205.
114. Fukuda, K.; Akatsuka, K.; Ebina, Y.; Ma, R.; Takada, K.; Nakai, I.; Sasaki, T. Exfoliated Nanosheet Crystallite of Cesium Tungstate with 2D Pyrochlore Structure: Synthesis, Characterization, and Photochromic Properties. *ACS Nano* **2008**, *2*, 1689–1695.
115. Akatsuka, K.; Haga, M.-a.; Ebina, Y.; Osada, M.; Fukuda, K.; Sasaki, T. Construction of Highly Ordered Lamellar Nanostructures through Langmuir–Blodgett Deposition of Molecularly Thin Titania Nanosheets Tens of Micrometers Wide and Their Excellent Dielectric Properties. *ACS Nano* **2009**, *3*, 1097–1106.
116. Osada, M.; Sasaki, T. Two-Dimensional Dielectric Nanosheets: Novel Nanoelectronics from Nanocrystal Building Blocks. *Adv. Mater.* **2012**, *24*, 210–228.
117. Osada, M.; Akatsuka, K.; Ebina, Y.; Kotani, Y.; Ono, K.; Funakubo, H.; Ueda, S.; Kobayashi, K.; Takada, K.; Sasaki, T. Langmuir–Blodgett Fabrication of Nanosheet-Based Dielectric Films without an Interfacial Dead Layer. *Jpn. J. Appl. Phys.* **2008**, *47*, 7556.
118. Osada, M.; Takanashi, G.; Li, B. W.; Akatsuka, K.; Ebina, Y.; Ono, K.; Funakubo, H.; Takada, K.; Sasaki, T. Controlled Polarizability of One-Nanometer-Thick Oxide Nanosheets for Tailored, High- κ Nanodielectrics. *Adv. Funct. Mater.* **2011**, *21*, 3482–3487.
119. Aksit, M.; Toledo, D. P.; Robinson, R. D. Scalable Nanomanufacturing of Millimetre-Length 2D Na_xCoO_2 Nanosheets. *J. Mater. Chem.* **2012**, *22*, 5936–5944.
120. Novoselov, K. S.; Geim, A. K.; Morozov, S. V.; Jiang, D.; Katsnelson, M. I.; Grigorieva, I. V.; Dubonos, S. V.; Firsov, A. A. Two-Dimensional Gas of Massless Dirac Fermions in Graphene. *Nature* **2005**, *438*, 197–200.
121. Lui, C. H.; Liu, L.; Mak, K. F.; Flynn, G. W.; Heinz, T. F. Ultraflat Graphene. *Nature* **2009**, *462*, 339–341.
122. Late, D. J.; Liu, B.; Matte, H.; Rao, C. N. R.; Dravid, V. P. Rapid Characterization of Ultrathin Layers of Chalcogenides on SiO_2/Si Substrates. *Adv. Funct. Mater.* **2012**, *22*, 1894–1905.
123. Benameur, M. M.; Radisavljevic, B.; Heron, J. S.; Sahoo, S.; Berger, H.; Kis, A. Visibility of Dichalcogenide Nanolayers. *Nanotechnology* **2011**, *22*, 5.
124. Blake, P.; Hill, E. W.; Neto, A. H. C.; Novoselov, K. S.; Jiang, D.; Yang, R.; Booth, T. J.; Geim, A. K. Making Graphene Visible. *Appl. Phys. Lett.* **2007**, *91*, 063124.
125. Splendiani, A.; Sun, L.; Zhang, Y.; Li, T.; Kim, J.; Chim, C. Y.; Galli, G.; Wang, F. Emerging Photoluminescence in Monolayer MoS_2 . *Nano Lett.* **2010**, *10*, 1271–1275.
126. Kim, J.; Cote, L. J.; Kim, F.; Huang, J. Visualizing Graphene Based Sheets by Fluorescence Quenching Microscopy. *J. Am. Chem. Soc.* **2010**, *132*, 260–267.
127. Kim, J.; Kim, F.; Huang, J. X. Seeing Graphene-Based Sheets. *Mater. Today* **2010**, *13*, 28–38.
128. Tan, A. L. T.; Kim, J.; Huang, J.-K.; Li, L.-J.; Huang, J. Seeing 2D Sheets on Arbitrary Substrates by Fluorescence Quenching Microscopy. *Small* **2013**, DOI: 10.1002/sml.201300049.
129. Dresselhaus, M. S.; Jorio, A.; Saito, R. In Characterizing Graphene, Graphite, and Carbon Nanotubes by Raman Spectroscopy. *Annual Review of Condensed Matter Physics*; Langer, J. S., Ed.; Annual Reviews: Palo Alto, CA, 2010; Vol. 1, pp 89–108.
130. Nemes-Incze, P.; Osvath, Z.; Kamaras, K.; Biro, L. P. Anomalies in Thickness Measurements of Graphene and Few Layer Graphite Crystals by Tapping Mode Atomic Force Microscopy. *Carbon* **2008**, *46*, 1435–1442.
131. Teweldebrhan, D.; Goyal, V.; Balandin, A. A. Exfoliation and Characterization of Bismuth Telluride Atomic Quintuples and Quasi-Two-Dimensional Crystals. *Nano Lett.* **2010**, *10*, 1209–1218.
132. Robinson, R. D.; Spanier, J. E.; Zhang, F.; Chan, S. W.; Herman, I. P. Visible Thermal Emission from Sub-Band-Gap Laser Excited Cerium Dioxide Particles. *J. Appl. Phys.* **2002**, *92*, 1936–1941.
133. Coleman, J. N.; Lotya, M.; O'Neill, A.; Bergin, S. D.; King, P. J.; Khan, U.; Young, K.; Gaucher, A.; De, S.; Smith, R. J.; et al. Two-Dimensional Nanosheets Produced by Liquid Exfoliation of Layered Materials. *Science* **2011**, *331*, 568–571.
134. McCombe, B. D. A History of Narrow Gap Semiconductors and Systems: From Graphite to Graphene. In *15th International Conference on Narrow Gap Systems*; Khodaparast, G. A., Santos, M. B., Stanton, C. J., Eds.; American Institute of Physics: College Park, MD, **2011**; Vol. 1416, p 9–13.
135. Gutiérrez, H. R.; Perea-López, N.; Elías, A. L.; Berkdemir, A.; Wang, B.; Lv, R.; López-Urías, F.; Crespi, V. H.; Terrones, M. Extraordinary Room-Temperature Photoluminescence in WS_2 Monolayers. *Nano Lett.* **2012**, DOI: 10.1021/nl3026357.
136. Ping, J. L.; Fuhrer, M. S. Layer Number and Stacking Sequence Imaging of Few-Layer Graphene by Transmission Electron Microscopy. *Nano Lett.* **2012**, *12*, 4635–4641.
137. Li, G.; Andrei, E. Y. Observation of Landau Levels of Dirac Fermions in Graphite. *Nat. Phys.* **2007**, *3*, 623–627.
138. Miller, D. L.; Kubista, K. D.; Rutter, G. M.; Ruan, M.; de Heer, W. A.; First, P. N.; Strosio, J. A. Observing the Quantization of Zero Mass Carriers in Graphene. *Science* **2009**, *324*, 924–927.
139. Helveg, S.; Lauritsen, J. V.; Laegsgaard, E.; Stensgaard, I.; Nørskov, J. K.; Clausen, B. S.; Topsoe, H.; Besenbacher, F. Atomic-Scale Structure of Single-Layer MoS_2 Nanoclusters. *Phys. Rev. Lett.* **2000**, *84*, 951–954.
140. Auwärter, W.; Kreutz, T. J.; Greber, T.; Osterwalder, J. XPD and STM Investigation of Hexagonal Boron Nitride on $\text{Ni}(111)$. *Surf. Sci.* **1999**, *429*, 229–236.
141. Brar, V. W.; Decker, R.; Solowan, H. M.; Wang, Y.; Maserati, L.; Chan, K. T.; Lee, H.; Girit, C. O.; Zettl, A.; Louie, S. G.; et al. Gate-Controlled Ionization and Screening of Cobalt Adatoms on a Graphene Surface. *Nat. Phys.* **2011**, *7*, 43–47.
142. Gyamfi, M.; Elbo, T.; Wasniowska, M.; Wiesendanger, R. Fe Adatoms on Graphene/ $\text{Ru}(0001)$: Adsorption Site and Local Electronic Properties. *Phys. Rev. B* **2011**, *84*, 4.
143. Brihuega, I.; Michaelis, C. H.; Zhang, J.; Bose, S.; Sessi, V.; Honolka, J.; Schneider, M. A.; Enders, A.; Kern, K. Electronic Decoupling and Templating of Co Nanocluster Arrays on the Boron Nitride Nanomesh. *Surf. Sci.* **2008**, *602*, L95–L99.
144. Natterer, F. D.; Patthey, F.; Brune, H. Ring State for Single Transition Metal Atoms on Boron Nitride on $\text{Rh}(111)$. *Phys. Rev. Lett.* **2012**, *109*, 066101.
145. Besenbacher, F.; Lauritsen, J. V.; Linderth, T. R.; Laegsgaard, E.; Vang, R. T.; Wendt, S. Atomic-Scale Surface Science Phenomena Studied by Scanning Tunneling Microscopy. *Surf. Sci.* **2009**, *603*, 1315–1327.
146. Ebina, Y.; Sasaki, T.; Watanabe, M. Study on Exfoliation of Layered Perovskite-Type Niobates. *Solid State Ionics* **2002**, *151*, 177–182.
147. Ding, Z.; Bux, S. K.; King, D. J.; Chang, F. L.; Chen, T.-H.; Huang, S.-C.; Kaner, R. B. Lithium Intercalation and Exfoliation of Layered Bismuth Selenide and Bismuth Telluride. *J. Mater. Chem.* **2009**, *19*, 2588–2592.
148. Wang, Q. H.; Kalantar-Zadeh, K.; Kis, A.; Coleman, J. N.; Strano, M. S. Electronics and Optoelectronics of Two-Dimensional Transition Metal Dichalcogenides. *Nat. Nanotechnol.* **2012**, *7*, 699–712.
149. Mak, K. F.; Lee, C.; Hone, J.; Shan, J.; Heinz, T. F. Atomically Thin MoS_2 : A New Direct-Gap Semiconductor. *Phys. Rev. Lett.* **2010**, *105*, 136805.
150. Lee, C.; Yan, H.; Brus, L. E.; Heinz, T. F.; Hone, J.; Ryu, S. Anomalous Lattice Vibrations of Single- and Few-Layer MoS_2 . *ACS Nano* **2010**, *4*, 2695–2700.
151. Korn, T.; Heydrich, S.; Hirmer, M.; Schmutzler, J.; Schueller, C. Low-Temperature Photocarrier Dynamics in Monolayer MoS_2 . *Appl. Phys. Lett.* **2011**, *99*, 102109.
152. Eda, G.; Yamaguchi, H.; Vohry, D.; Fujita, T.; Chen, M.; Chhowalla, M. Photoluminescence from Chemically Exfoliated MoS_2 . *Nano Lett.* **2012**, *12*, 526–526.

153. Mak, K. F.; He, K.; Shan, J.; Heinz, T. F. Control of Valley Polarization in Monolayer MoS₂ by Optical Helicity. *Nat. Nanotechnol.* **2012**, *7*, 494–498.
154. Cao, T.; Wang, G.; Han, W.; Ye, H.; Zhu, C.; Shi, J.; Niu, Q.; Tan, P.; Wang, P.; Liu, B.; et al. Valley-Selective Circular Dichroism of Monolayer Molybdenum Disulphide. *Nat. Commun.* **2012**, *3*, 887.
155. Zeng, H.; Dai, J.; Yao, W.; Xiao, D.; Cui, X. Valley Polarization in MoS₂ Monolayers by Optical Pumping. *Nat. Nanotechnol.* **2012**, *7*, 490–493.
156. Mak, K. F.; He, K.; Lee, C.; Lee, G. H.; Hone, J.; Heinz, T. F.; Shan, J. Tightly Bound Trions in Monolayer MoS₂. *Nat. Mater.* **2013**, *12*, 207–211.
157. Ross, J. S.; Wu, S.; Yu, H.; Ghimire, N. J.; Jones, A. M.; Aivazian, G.; Morasch, J.; Yan, J.; Mandrus, D. G.; Xiao, D.; et al. Electrical Control of Neutral and Charged Excitons in 2D Crystals. *Nat. Commun.* **2013**, DOI: 10.1038/ncomms2498.
158. Sallen, G.; Bouet, L.; Marie, X.; Wang, G.; Zhu, C. R.; Han, W. P.; Lu, Y.; Tan, P. H.; Amand, T.; Liu, B. L.; et al. Robust Optical Emission Polarization in MoS₂ Monolayers through Selective Valley Excitation. *Phys. Rev. B* **2012**, *86*, 081301.
159. Wang, R.; Ruzicka, B. A.; Kumar, N.; Bellus, M. Z.; Chiu, H.-Y.; Zhao, H. Ultrafast and Spatially Resolved Studies of Charge Carriers in Atomically Thin Molybdenum Disulfide. *Phys. Rev. B* **2012**, *86*, 045406.
160. Najmaei, S.; Liu, Z.; Ajayan, P. M.; Lou, J. Thermal Effects on the Characteristic Raman Spectrum of Molybdenum Disulfide (MoS₂) of Varying Thicknesses. *Appl. Phys. Lett.* **2012**, *100*, 013106.
161. Newaz, A. K. M.; Prasai, D.; Ziegler, J. I.; Caudel, D.; Robinson, S.; Hagland, R. F., Jr.; Bolotin, K. I. Electrical Control of Optical Properties of Monolayer MoS₂. *Solid State Communications* **2013**, *155*, 49–52.
162. Ayari, A.; Cobas, E.; Ogundadege, O.; Fuhrer, M. S. Realization and Electrical Characterization of Ultrathin Crystals of Layered Transition-Metal Dichalcogenides. *J. Appl. Phys.* **2007**, *101*, 014507.
163. Radisavljevic, B.; Radenovic, A.; Brivio, J.; Giacometti, V.; Kis, A. Single-Layer MoS₂ Transistors. *Nat. Nanotechnol.* **2011**, *6*, 147–150.
164. Yoon, Y.; Ganapathi, K.; Salahuddin, S. How Good Can Monolayer MoS₂ Transistors Be? *Nano Lett.* **2011**, *11*, 3768–3773.
165. Radisavljevic, B.; Whitwick, M. B.; Kis, A. Integrated Circuits and Logic Operations Based on Single-Layer MoS₂. *ACS Nano* **2011**, *5*, 9934–9938.
166. Ghatak, S.; Pal, A. N.; Ghosh, A. Nature of Electronic States in Atomically Thin MoS₂ Field-Effect Transistors. *ACS Nano* **2011**, *5*, 7707–7712.
167. Radisavljevic, B.; Whitwick, M. B.; Kis, A. Small-Signal Amplifier Based on Single-Layer MoS₂. *Appl. Phys. Lett.* **2012**, *101*, 043103.
168. Liu, H.; Ye, P. D. MoS₂ Dual-Gate MOSFET with Atomic-Layer-Deposited Al₂O₃ as Top-Gate Dielectric. *IEEE Electron Device Lett.* **2012**, *33*, 546–548.
169. Wang, H.; Yu, L.; Lee, Y.-H.; Shi, Y.; Hsu, A.; Chin, M. L.; Li, L.-J.; Dubey, M.; Kong, J.; Palacios, T. Integrated Circuits Based on Bilayer MoS₂ Transistors. *Nano Lett.* **2012**, *12*, 4674–4680.
170. Lin, M.-W.; Liu, L.; Lan, Q.; Tan, X.; Dhindsa, K. S.; Zeng, P.; Naik, V. M.; Cheng, M. M.-C.; Zhou, Z. Mobility Enhancement and Highly Efficient Gating of Monolayer MoS₂ Transistors with Polymer Electrolyte. *J. Phys. D: Appl. Phys.* **2012**, *45*, 345102.
171. Britnell, L.; Gorbachev, R. V.; Jalil, R.; Belle, B. D.; Schedin, F.; Mishchenko, A.; Georgiou, T.; Katsnelson, M. I.; Eaves, L.; Morozov, S. V.; et al. Field-Effect Tunneling Transistor Based on Vertical Graphene Heterostructures. *Science* **2012**, *335*, 947–950.
172. Lembke, D.; Kis, A. Breakdown of High-Performance Monolayer MoS₂ Transistors. *ACS Nano* **2012**, *6*, 10070–10075.
173. Yin, Z.; Li, H.; Li, H.; Jiang, L.; Shi, Y.; Sun, Y.; Lu, G.; Zhang, Q.; Chen, X.; Zhang, H. Single-Layer MoS₂ Phototransistors. *ACS Nano* **2012**, *6*, 74–80.
174. Zhan, Y.; Liu, Z.; Najmaei, S.; Ajayan, P. M.; Lou, J. Large-Area Vapor-Phase Growth and Characterization of MoS₂ Atomic Layers on a SiO₂ Substrate. *Small* **2012**, *8*, 966–971.
175. Lee, Y.-H.; Zhang, X.-Q.; Zhang, W.; Chang, M.-T.; Lin, C.-T.; Chang, K.-D.; Yu, Y.-C.; Wang, J. T.-W.; Chang, C.-S.; Li, L.-J.; et al. Synthesis of Large-Area MoS₂ Atomic Layers with Chemical Vapor Deposition. *Adv. Mater.* **2012**, *24*, 2320–2325.
176. Mattheis, L. Band Structures of Transition Metal Dichalcogenide Layer Compounds. *Phys. Rev. B* **1973**, *8*, 3719–3740.
177. Ellis, J. K.; Lucero, M. J.; Scuseria, G. E. The Indirect to Direct Band Gap Transition in Multilayered MoS₂ As Predicted by Screened Hybrid Density Functional Theory. *Appl. Phys. Lett.* **2011**, *99*, 261908.
178. Cheiwchanchamnangij, T.; Lambrecht, W. R. L. Quasiparticle Band Structure Calculation of Monolayer, Bilayer, and Bulk MoS₂. *Phys. Rev. B* **2012**, *85*, 205302.
179. Kumar, A.; Ahluwalia, P. K. Electronic Structure of Transition Metal Dichalcogenides Monolayers 1H-MX₂ (M = Mo, W; X = S, Se, Te) from *Ab-Initio* Theory: New Direct Band Gap Semiconductors. *Eur. Phys. J. B* **2012**, *85*, 186–187.
180. Komsa, H.-P.; Krasheninnikov, A. V. Effects of Confinement and Environment on the Electronic Structure and Exciton Binding Energy of MoS₂ from First Principles. *Phys. Rev. B* **2012**, *86*, 241201.
181. Komsa, H.-P.; Krasheninnikov, A. V. Two-Dimensional Transition Metal Dichalcogenide Alloys: Stability and Electronic Properties. *J. Phys. Chem. Lett.* **2012**, *3*, 3652–3656.
182. Ramasubramanian, A. Large Excitonic Effects in Monolayers of Molybdenum and Tungsten Dichalcogenides. *Phys. Rev. B* **2012**, *86*, 115409.
183. Scalise, E.; Houssa, M.; Pourtois, G.; Afanas'ev, V. V.; Stesmans, A. Strain-Induced Semiconductor to Metal Transition in the Two-Dimensional Honeycomb Structure of MoS₂. *Nano Res.* **2012**, *5*, 43–48.
184. Yun, W. S.; Han, S. W.; Hong, S. C.; Kim, I. G.; Lee, J. D. Thickness and Strain Effects on Electronic Structures of Transition Metal Dichalcogenides: 2H-M X-2 Semiconductors (M = Mo, W; X = S, Se, Te). *Phys. Rev. B* **2012**, *85*, 033305.
185. Feng, J.; Qian, X.; Huang, C.-W.; Li, J. Strain-Engineered Artificial Atom as a Broad-Spectrum Solar Energy Funnel. *Nat. Photonics* **2012**, *6*, 865–871.
186. Peelaers, H.; Van de Walle, C. G. Effects of Strain on Band Structure and Effective Masses in MoS₂. *Phys. Rev. B* **2012**, *86*, 241401.
187. Evans, B. L.; Young, P. A. Optical Absorption and Dispersion in Molybdenum Disulphide. *Proc. R. Soc. A* **1965**, *284*, 402–422.
188. Zhu, Z. Y.; Cheng, Y. C.; Schwingenschloegl, U. Giant Spin-Orbit-Induced Spin Splitting in Two-Dimensional Transition-Metal Dichalcogenide Semiconductors. *Phys. Rev. B* **2011**, *84*, 153402.
189. Botello-Mendez, A. R.; Lopez-Urias, F.; Terrones, M.; Terrones, H. Metallic and Ferromagnetic Edges in Molybdenum Disulfide Nanoribbons. *Nanotechnology* **2009**, *20*, 325703.
190. Zou, X.; Liu, Y.; Jakobson, B. I. Predicting Dislocations and Grain Boundaries in Two-Dimensional Metal-Disulfides from the First Principles. *Nano Lett.* **2012**, *13*, 253–258.
191. Ma, Y. D.; Dai, Y.; Guo, M.; Niu, C. W.; Lu, J. B.; Huang, B. B. Electronic and Magnetic Properties of Perfect, Vacancy-Doped, and Nonmetal Adsorbed MoSe₂, MoTe₂ and WS₂ Monolayers. *Phys. Chem. Chem. Phys.* **2011**, *13*, 15546–15553.
192. Bollinger, M. V.; Lauritsen, J. V.; Jacobsen, K. W.; Norskov, J. K.; Helveg, S.; Besenbacher, F. One-Dimensional Metallic Edge States in MoS₂. *Phys. Rev. Lett.* **2001**, *87*, 196803.
193. Lauritsen, J. V.; Kibsgaard, J.; Helveg, S.; Topsoe, H.; Clausen, B. S.; Laegsgaard, E.; Besenbacher, F. Size-Dependent Structure of MoS₂ Nanocrystals. *Nat. Nanotechnol.* **2007**, *2*, 53–58.
194. Jaramillo, T. F.; Jorgensen, K. P.; Bonde, J.; Nielsen, J. H.; Horch, S.; Chorkendorff, I. Identification of Active Edge

- Sites for Electrochemical H-2 Evolution from MoS₂ Nanocatalysts. *Science* **2007**, *317*, 100–102.
195. Lee, Y. H.; Zhang, X. Q.; Zhang, W. J.; Chang, M. T.; Lin, C. T.; Chang, K. D.; Yu, Y. C.; Wang, J. T. W.; Chang, C. S.; Li, L. J.; *et al.* Synthesis of Large-Area MoS₂ Atomic Layers with Chemical Vapor Deposition. *Adv. Mater.* **2012**, *24*, 2320–2325.
196. Li, H.; Zhang, Q.; Yap, C. C. R.; Tay, B. K.; Edwin, T. H. T.; Olivier, A.; Baillargeat, D. From Bulk to Monolayer MoS₂: Evolution of Raman Scattering. *Adv. Funct. Mater.* **2012**, *22*, 1385–1390.
197. Liu, K. K.; Zhang, W. J.; Lee, Y. H.; Lin, Y. C.; Chang, M. T.; Su, C.; Chang, C. S.; Li, H.; Shi, Y. M.; Zhang, H.; *et al.* Growth of Large-Area and Highly Crystalline MoS₂ Thin Layers on Insulating Substrates. *Nano Lett.* **2012**, *12*, 1538–1544.
198. Mak, K. F.; He, K.; Shan, J.; Heinz, T. F. Control of Valley Polarization in Monolayer MoS₂ by Optical Helicity. *Nat. Nanotechnol.* **2012**, *7*, 494–498.
199. Bertram, N.; Cordes, J.; Kim, Y. D.; Gantefor, G.; Gemming, S.; Seifert, G. Nanoplatelets Made from MoS₂ and WS₂. *Chem. Phys. Lett.* **2006**, *418*, 36–39.
200. Matte, H. S. S. R.; Gomathi, A.; Manna, A. K.; Late, D. J.; Datta, R.; Pati, S. K.; Rao, C. N. R. MoS₂ and WS₂ Analogues of Graphene. *Angew. Chem., Int. Ed.* **2010**, *49*, 4059–4062.
201. Ding, Y.; Wang, Y. L.; Ni, J.; Shi, L.; Shi, S. Q.; Tang, W. H. First Principles Study of Structural, Vibrational and Electronic Properties of Graphene-like MX₂ (M = Mo, Nb, W, Ta; X = S, Se, Te) Monolayers. *Physica B* **2011**, *406*, 2254–2260.
202. Molina-Sanchez, A.; Wirtz, L. Phonons in Single-Layer and Few-Layer MoS₂ and WS₂. *Phys. Rev. B* **2011**, *84*, 155413.
203. Martins, T. B.; Miwa, R. H.; da Silva, A. J. R.; Fazzio, A. Electronic and Transport Properties of Boron-Doped Graphene Nanoribbons. *Phys. Rev. Lett.* **2007**, *98*, 196803.
204. Wei, D. C.; Liu, Y. Q.; Wang, Y.; Zhang, H. L.; Huang, L. P.; Yu, G. Synthesis of N-Doped Graphene by Chemical Vapor Deposition and Its Electrical Properties. *Nano Lett.* **2009**, *9*, 1752–1758.
205. Terrones, H.; Lv, R.; Terrones, M.; Dresselhaus, M. S. The Role of Defects and Doping in 2D Graphene Sheets and 1D Nanoribbons. *Rep. Prog. Phys.* **2012**, *75*, 062501.
206. Yan, Q.; Huang, B.; Yu, J.; Zheng, F.; Zang, J.; Wu, J.; Gu, B.-L.; Liu, F.; Duan, W. Intrinsic Current–Voltage Characteristics of Graphene Nanoribbon Transistors and Effect of Edge Doping. *Nano Lett.* **2007**, *7*, 1469–1473.
207. Wang, X. R.; Li, X. L.; Zhang, L.; Yoon, Y.; Weber, P. K.; Wang, H. L.; Guo, J.; Dai, H. J. N-Doping of Graphene through Electrothermal Reactions with Ammonia. *Science* **2009**, *324*, 768–771.
208. Moser, J.; Barchiesi, A.; Bachtold, A. Current-Induced Cleaning of Graphene. *Appl. Phys. Lett.* **2007**, *91*, 163513.
209. Chisholm, M. F.; Duschner, G.; Windl, W. Oxidation Resistance of Reactive Atoms in Graphene. *Nano Lett.* **2012**, *12*, 4651–4655.
210. Elias, D. C.; Nair, R. R.; Mohiuddin, T. M. G.; Morozov, S. V.; Blake, P.; Halsall, M. P.; Ferrari, A. C.; Boukhvalov, D. W.; Katsnelson, M. I.; Geim, A. K.; *et al.* Control of Graphene's Properties by Reversible Hydrogenation: Evidence for Graphane. *Science* **2009**, *323*, 610–613.
211. Nair, R. R.; Ren, W. C.; Jalil, R.; Riaz, I.; Kravets, V. G.; Britnell, L.; Blake, P.; Schedin, F.; Mayorov, A. S.; Yuan, S. J.; *et al.* Fluorographene: A Two-Dimensional Counterpart of Teflon. *Small* **2010**, *6*, 2877–2884.
212. Fuentes-Cabrera, M.; Munoz, A.; Windl, W.; Demkov, A. A.; Sankey, O. F. Theoretical Study of Graphitic Analogues of Simple Semiconductors. *Modell. Simul. Mater. Sci. Eng.* **1999**, *7*, 929–938.
213. Van de Walle, C. G.; Northrup, J. E. First-Principles Investigation of Visible Light Emission from Silicon-Based Materials. *Phys. Rev. Lett.* **1993**, *70*, 1116–1119.
214. Voon, L. C. L. Y.; Sandberg, E.; Aga, R. S.; Farajian, A. A. Hydrogen Compounds of Group-IV Nanosheets. *Appl. Phys. Lett.* **2010**, *97*, 163114.
215. Osborn, T. H.; Farajian, A. A.; Pupyshcheva, O. V.; Aga, R. S.; Voon, L. C. L. Y. *Ab Initio* Simulations of Silicene Hydrogenation. *Chem. Phys. Lett.* **2011**, *511*, 101–105.
216. Garcia, J. C.; de Lima, D. B.; Assali, L. V. C.; Justo, J. F. Group IV Graphene- and Graphane-like Nanosheets. *J. Phys. Chem. C* **2011**, *115*, 13242–13246.
217. Houssa, M.; Scalise, E.; Sankaran, K.; Pourtois, G.; Afanas'ev, V. V.; Stesmans, A. Electronic Properties of Hydrogenated Silicene and Germanene. *Appl. Phys. Lett.* **2011**, *98*, 223107.
218. Ding, Y.; Wang, Y. L. Electronic Structures of Silicene Fluoride and Hydride. *Appl. Phys. Lett.* **2012**, *100*, 083102.
219. Gao, N.; Zheng, W. T.; Jiang, Q. Density Functional Theory Calculations for Two-Dimensional Silicene with Halogen Functionalization. *Phys. Chem. Chem. Phys.* **2012**, *14*, 257–261.
220. Hajnal, Z.; Vogg, G.; Meyer, L. J. P.; Szucs, B.; Brandt, M. S.; Frauenheim, T. Band Structure and Optical Properties of Germanium Sheet Polymers. *Phys. Rev. B* **2001**, *64*, 033311.
221. Restrepo, O. D. M. R.; Goldberger, J. E.; Windl, W. The Transition in Band Structure from Silicon to Silicene to Silicane. Manuscript in preparation.
222. Heyd, J.; Scuseria, G. E.; Ernzerhof, M. Hybrid Functionals Based on a Screened Coulomb Potential. *J. Chem. Phys.* **2003**, *118*, 8207–8215.
223. Paier, J.; Marsman, M.; Hummer, K.; Kresse, G.; Gerber, I. C.; Angyan, J. G. Screened Hybrid Density Functionals Applied to Solids. *J. Chem. Phys.* **2006**, *124*, 154709.
224. Pulizzi, F. Spintronics. *Nat. Mater.* **2012**, *11*, 367–367.
225. Wolf, S. A.; Awschalom, D. D.; Buhrman, R. A.; Daughton, J. M.; von Molnár, S.; Roukes, M. L.; Chtchelkanova, A. Y.; Treger, D. M. Spintronics: A Spin-Based Electronics Vision for the Future. *Science* **2001**, *294*, 1488–1495.
226. Tombros, N.; Jozsa, C.; Popinciuc, M.; Jonkman, H. T.; van Wees, B. J. Electronic Spin Transport and Spin Precession in Single Graphene Layers at Room Temperature. *Nature* **2007**, *448*, 571–574.
227. Han, W.; Pi, K.; Wang, W. H.; McCreary, K. M.; Li, Y.; Bao, W.; Wei, P.; Shi, J.; Lau, C. N.; Kawakami, R. K. Spin Transport in Graphite and Graphene Spin Valves. *Proc. SPIE* **2009**, *7398*, 739819–739819-11.
228. Han, W.; Kawakami, R. K. Spin Relaxation in Single-Layer and Bilayer Graphene. *Phys. Rev. Lett.* **2011**, *107*, 047207.
229. Han, W.; Pi, K.; McCreary, K. M.; Li, Y.; Wong, J. J. I.; Swartz, A. G.; Kawakami, R. K. Tunneling Spin Injection into Single Layer Graphene. *Phys. Rev. Lett.* **2010**, *105*, 167202.
230. Kim, W. Y.; Kim, K. S. Prediction of Very Large Values of Magnetoresistance in a Graphene Nanoribbon Device. *Nat. Nanotechnol.* **2008**, *3*, 408–412.
231. Xiao, D.; Liu, G.-B.; Feng, W.; Xu, X.; Yao, W. Coupled Spin and Valley Physics in Monolayers of MoS₂ and Other Group-VI Dichalcogenides. *Phys. Rev. Lett.* **2012**, *108*, 196802.
232. Xiao, D.; Yao, W.; Niu, Q. Valley-Contrasting Physics in Graphene: Magnetic Moment and Topological Transport. *Phys. Rev. Lett.* **2007**, *99*, 236809.
233. Gunawan, O.; Shkolnikov, Y. P.; Vakili, K.; Gokmen, T.; De Poortere, E. P.; Shayegan, M. Valley Susceptibility of an Interacting Two-Dimensional Electron System. *Phys. Rev. Lett.* **2006**, *97*, 186404.
234. Haigh, S. J.; Gholinia, A.; Jalil, R.; Romani, S.; Britnell, L.; Elias, D. C.; Novoselov, K. S.; Ponomarenko, L. A.; Geim, A. K.; Gorbachev, R. Cross-Sectional Imaging of Individual Layers and Buried Interfaces of Graphene-Based Heterostructures and Superlattices. *Nat. Mater.* **2012**, *11*, 764–767.
235. Linder, J.; Sudbo, A. Dirac Fermions and Conductance Oscillations in S- and D-Wave Superconductor-Graphene Junctions. *Phys. Rev. Lett.* **2007**, *99*, 147001.
236. Renk, K. F.; Stahl, B. I.; Rogl, A.; Janzen, T.; Pavel'ev, D. G.; Koshurinov, Y. I.; Ustinov, V.; Zhukov, A. Subterahertz Superlattice Parametric Oscillator. *Phys. Rev. Lett.* **2005**, *95*, 126801.
237. Chen, H. T.; Padilla, W. J.; Zide, J. M. O.; Bank, S. R.; Gossard, A. C.; Taylor, A. J.; Averitt, R. D. Ultrafast Optical Switching of Terahertz Metamaterials Fabricated on ErAs/GaAs Nanoisland Superlattices. *Opt. Lett.* **2007**, *32*, 1620–1622.
238. Pimenov, A.; Loidl, A.; Przyslupski, P.; Dabrowski, B. Negative Refraction in Ferromagnet-Superconductor Superlattices. *Phys. Rev. Lett.* **2005**, *95*, 247009.

239. Giovannetti, G.; Khomyakov, P. A.; Brocks, G.; Kelly, P. J.; van den Brink, J. Substrate-Induced Band Gap in Graphene on Hexagonal Boron Nitride: *Ab Initio* Density Functional Calculations. *Phys. Rev. B* **2007**, *76*, 073103.
240. Fan, Y.; Zhao, M.; Wang, Z.; Zhang, X.; Zhang, H. Tunable Electronic Structures of Graphene/Boron Nitride Heterobilayers. *Appl. Phys. Lett.* **2011**, *98*, 083103.
241. Dean, C. R.; Young, A. F.; Meric, I.; Lee, C.; Wang, L.; Sorgenfrei, S.; Watanabe, K.; Taniguchi, T.; Kim, P.; Shepard, K. L.; *et al.* Boron Nitride Substrates for High-Quality Graphene Electronics. *Nat. Nanotechnol.* **2010**, *5*, 722–726.
242. Mayorov, A. S.; Gorbachev, R. V.; Morozov, S. V.; Britnell, L.; Jalil, R.; Ponomarenko, L. A.; Blake, P.; Novoselov, K. S.; Watanabe, K.; Taniguchi, T.; *et al.* Micrometer-Scale Ballistic Transport in Encapsulated Graphene at Room Temperature. *Nano Lett.* **2011**, *11*, 2396–2399.
243. Cheianov, V. V.; Fal'ko, V. I.; Altshuler, B. L.; Aleiner, I. L. Random Resistor Network Model of Minimal Conductivity in Graphene. *Phys. Rev. Lett.* **2007**, *99*, 176801.
244. Ponomarenko, L. A.; Geim, A. K.; Zhukov, A. A.; Jalil, R.; Morozov, S. V.; Novoselov, K. S.; Grigorieva, I. V.; Hill, E. H.; Cheianov, V. V.; Fal'ko, V. I.; *et al.* Tunable Metal-Insulator Transition in Double-Layer Graphene Heterostructures. *Nat. Phys.* **2011**, *7*, 958–961.
245. Decker, R.; Wang, Y.; Brar, V. W.; Regan, W.; Tsai, H. Z.; Wu, Q.; Gannett, W.; Zettl, A.; Crommie, M. F. Local Electronic Properties of Graphene on a BN Substrate via Scanning Tunneling Microscopy. *Nano Lett.* **2011**, *11*, 2291–2295.
246. Fu, L.; Kane, C. L.; Mele, E. J. Topological Insulators in Three Dimensions. *Phys. Rev. Lett.* **2007**, *98*, 106803.
247. Hsieh, D.; Xia, Y.; Wray, L.; Qian, D.; Pal, A.; Dil, J. H.; Osterwalder, J.; Meier, F.; Bihlmayer, G.; Kane, C. L.; *et al.* Observation of Unconventional Quantum Spin Textures in Topological Insulators. *Science* **2009**, *323*, 919–922.
248. Roushan, P.; Seo, J.; Parker, C. V.; Hor, Y. S.; Hsieh, D.; Qian, D.; Richardella, A.; Hasan, M. Z.; Cava, R. J.; Yazdani, A. Topological Surface States Protected from Backscattering by Chiral Spin Texture. *Nature* **2009**, *460*, 1106–U1164.
249. Hsieh, D.; Qian, D.; Wray, L.; Xia, Y.; Hor, Y. S.; Cava, R. J.; Hasan, M. Z. A Topological Dirac Insulator in a Quantum Spin Hall Phase. *Nature* **2008**, *452*, 970–U975.
250. Zhang, H. J.; Liu, C. X.; Qi, X. L.; Dai, X.; Fang, Z.; Zhang, S. C. Topological Insulators in Bi_2Se_3 , Bi_2Te_3 and Sb_2Te_3 with a Single Dirac Cone on the Surface. *Nat. Phys.* **2009**, *5*, 438–442.
251. Xia, Y.; Qian, D.; Hsieh, D.; Wray, L.; Pal, A.; Lin, H.; Bansil, A.; Grauer, D.; Hor, Y. S.; Cava, R. J.; *et al.* Observation of a Large-Gap Topological-Insulator Class with a Single Dirac Cone on the Surface. *Nat. Phys.* **2009**, *5*, 398–402.
252. Chen, Y. L.; Analytis, J. G.; Chu, J. H.; Liu, Z. K.; Mo, S. K.; Qi, X. L.; Zhang, H. J.; Lu, D. H.; Dai, X.; Fang, Z.; *et al.* Experimental Realization of a Three-Dimensional Topological Insulator, Bi_2Te_3 . *Science* **2009**, *325*, 178–181.
253. Analytis, J. G.; McDonald, R. D.; Riggs, S. C.; Chu, J. H.; Boebinger, G. S.; Fisher, I. R. Two-Dimensional Surface State in the Quantum Limit of a Topological Insulator. *Nat. Phys.* **2010**, *6*, 960–964.
254. Peng, H. L.; Lai, K. J.; Kong, D. S.; Meister, S.; Chen, Y. L.; Qi, X. L.; Zhang, S. C.; Shen, Z. X.; Cui, Y. Aharonov–Bohm Interference in Topological Insulator Nanoribbons. *Nat. Mater.* **2010**, *9*, 225–229.
255. Kong, D. S.; Chen, Y. L.; Cha, J. J.; Zhang, Q. F.; Analytis, J. G.; Lai, K. J.; Liu, Z. K.; Hong, S. S.; Koski, K. J.; Mo, S. K.; *et al.* Ambipolar Field Effect in the Ternary Topological Insulator $(\text{Bi}_{1-x}\text{Sb}_x)_2\text{Te}_3$ by Composition Tuning. *Nat. Nanotechnol.* **2011**, *6*, 705–709.
256. Hong, S. S.; Cha, J. J.; Kong, D. S.; Cui, Y. Ultra-Low Carrier Concentration and Surface-Dominant Transport in Antimony-Doped Bi_2Se_3 Topological Insulator Nanoribbons. *Nat. Commun.* **2012**, *3*, 757.
257. Sacepe, B.; Oostinga, J. B.; Li, J.; Ubalini, A.; Couto, N. J. G.; Giannini, E.; Morpurgo, A. F. Gate-Tuned Normal and Superconducting Transport at the Surface of a Topological Insulator. *Nat. Commun.* **2011**, *2*, 575.
258. Moore, J. E. The Birth of Topological Insulators. *Nature* **2010**, *464*, 194–198.
259. Fu, L.; Kane, C. L. Superconducting Proximity Effect and Majorana Fermions at the Surface of a Topological Insulator. *Phys. Rev. Lett.* **2008**, *100*, 096407.
260. Hor, Y. S.; Richardella, A.; Roushan, P.; Xia, Y.; Checkelsky, J. G.; Yazdani, A.; Hasan, M. Z.; Ong, N. P.; Cava, R. J. p-Type Bi_2Se_3 for Topological Insulator and Low-Temperature Thermoelectric Applications. *Phys. Rev. B* **2009**, *79*, 195208.
261. Ghosh, S.; Bao, W.; Nika, D. L.; Subrina, S.; Pokatilov, E. P.; Lau, C. N.; Balandin, A. A. Dimensional Crossover of Thermal Transport in Few-Layer Graphene. *Nat. Mater.* **2010**, *9*, 555–558.
262. Chen, S. S.; Moore, A. L.; Cai, W. W.; Suk, J. W.; An, J. H.; Mishra, C.; Amos, C.; Magnuson, C. W.; Kang, J. Y.; Shi, L.; *et al.* Raman Measurements of Thermal Transport in Suspended Monolayer Graphene of Variable Sizes in Vacuum and Gaseous Environments. *ACS Nano* **2011**, *5*, 321–328.
263. Faugeras, C.; Faugeras, B.; Orlita, M.; Potemski, M.; Nair, R. R.; Geim, A. K. Thermal Conductivity of Graphene in Corbino Membrane Geometry. *ACS Nano* **2010**, *4*, 1889–1892.
264. Lee, J. U.; Yoon, D.; Kim, H.; Lee, S. W.; Cheong, H. Thermal Conductivity of Suspended Pristine Graphene Measured by Raman Spectroscopy. *Phys. Rev. B* **2011**, *83*, 081419.
265. Lindsay, L.; Broido, D. A.; Mingo, N. Flexural Phonons and Thermal Transport in Graphene. *Phys. Rev. B* **2010**, *82*, 6.
266. Lindsay, L.; Broido, D. A. Enhanced Thermal Conductivity and Isotope Effect in Single-Layer Hexagonal Boron Nitride. *Phys. Rev. B* **2011**, *84*, 155421.
267. Seol, J. H.; Jo, I.; Moore, A. L.; Lindsay, L.; Aitken, Z. H.; Pettes, M. T.; Li, X. S.; Yao, Z.; Huang, R.; Broido, D.; *et al.* Two-Dimensional Phonon Transport in Supported Graphene. *Science* **2010**, *328*, 213–216.
268. Jang, W. Y.; Chen, Z.; Bao, W. Z.; Lau, C. N.; Dames, C. Thickness-Dependent Thermal Conductivity of Encased Graphene and Ultrathin Graphite. *Nano Lett.* **2010**, *10*, 3909–3913.
269. Qiu, B.; Ruan, X. L. Reduction of Spectral Phonon Relaxation Times from Suspended to Supported Graphene. *Appl. Phys. Lett.* **2012**, *100*, 193101.
270. Pettes, M. T.; Jo, I. S.; Yao, Z.; Shi, L. Influence of Polymeric Residue on the Thermal Conductivity of Suspended Bilayer Graphene. *Nano Lett.* **2011**, *11*, 1195–1200.
271. Sadeghi, M. M.; Shi, L. Thermal Transport Measurements of Bilayer and Few-Layer Graphene Supported on Silicon Dioxide. In *Proceedings of the ASME 2011 International Mechanical Engineering Congress & Exposition*; ASME, Denver, CO, 2011; Vol. 10, pg 361–368, DOI: 10.1115/IMECE2011-64227.
272. Jo, I.; Pettes, M. T.; Kim, J. H.; Watanabe, K.; Taniguchi, T.; Yao, Z.; Shi, L. Thermal Conductivity and Phonon Transport in Suspended Few-Layer Hexagonal Boron Nitride. *Nano Lett.* **2013**, *13*, 550–554.
273. Chen, Z.; Jang, W.; Bao, W.; Lau, C. N.; Dames, C. Thermal Contact Resistance between Graphene and Silicon Dioxide. *Appl. Phys. Lett.* **2009**, *95*, 161910.
274. Koh, Y. K.; Bae, M. H.; Cahill, D. G.; Pop, E. Heat Conduction across Monolayer and Few-Layer Graphenes. *Nano Lett.* **2010**, *10*, 4363–4368.
275. Cai, W. W.; Moore, A. L.; Zhu, Y. W.; Li, X. S.; Chen, S. S.; Shi, L.; Ruoff, R. S. Thermal Transport in Suspended and Supported Monolayer Graphene Grown by Chemical Vapor Deposition. *Nano Lett.* **2010**, *10*, 1645–1651.
276. Mak, K. F.; Lui, C. H.; Heinz, T. F. Measurement of the Thermal Conductance of the Graphene/ SiO_2 Interface. *Appl. Phys. Lett.* **2010**, *97*, 221904.
277. Cullen, W. G.; Yamamoto, M.; Burson, K. M.; Chen, J. H.; Jang, C.; Li, L.; Fuhrer, M. S.; Williams, E. D. High-Fidelity Conformation of Graphene to SiO_2 Topographic Features. *Phys. Rev. Lett.* **2010**, *105*, 215504.
278. Duda, J. C.; Smoyer, J. L.; Norris, P. M.; Hopkins, P. E. Extension of the Diffuse Mismatch Model for Thermal Boundary Conductance between Isotropic and Anisotropic Materials. *Appl. Phys. Lett.* **2009**, *95*, 031912.

279. Vineis, C. J.; Shakouri, A.; Majumdar, A.; Kanatzidis, M. G. Nanostructured Thermoelectrics: Big Efficiency Gains from Small Features. *Adv. Mater.* **2010**, *22*, 3970–3980.
280. Shi, L. Thermal and Thermoelectric Transport in Nanostructures and Low-Dimensional Systems. *Nanoscale Microscale Thermophys. Eng.* **2012**, *16*, 79–116.
281. Hicks, L. D.; Dresselhaus, M. S. Thermoelectric Figure of Merit of a One-Dimensional Conductor. *Phys. Rev. B* **1993**, *47*, 16631–16634.
282. Hicks, L. D.; Dresselhaus, M. S. Effect of Quantum-Well Structures on the Thermoelectric Figure of Merit. *Phys. Rev. B* **1993**, *47*, 12727–12731.
283. Ghaemi, P.; Mong, R. S. K.; Moore, J. E. In-Plane Transport and Enhanced Thermoelectric Performance in Thin Films of the Topological Insulators Bi_2Te_3 and Bi_2Se_3 . *Phys. Rev. Lett.* **2010**, *105*, 166603.
284. Taur, Y.; Ning, T. H. *Fundamentals of Modern VLSI Devices*; Cambridge University Press: Cambridge, UK, 1998.
285. Yan, R. H.; Ourmazd, A.; Lee, K. F. Scaling the Si Mosfet—From Bulk to SOI to Bulk. *IEEE Trans. Electron Devices* **1992**, *39*, 1704–1710.
286. Majumdar, A.; Ren, Z. B.; Sleight, J. W.; Dobuzinsky, D.; Holt, J. R.; Venigalla, R.; Koester, S. J.; Haensch, W. High-Performance Undoped-Body 8-nm-Thin SOI Field-Effect Transistors. *IEEE Electron Device Lett.* **2008**, *29*, 515–517.
287. Datta, S. *Quantum Transport: Atom to Transistor*; Cambridge University Press: New York, 2006.
288. Knoch, J.; Appenzeller, J. Carbon Nanotube Field-Effect Transistors—The Importance of Being Small. In *Amiware Hardware Technology Drivers of Ambient Intelligence*; Mukherjee, S., Aarts, R., Roovers, R., Widdershoven, F., Ouwerkerk, M., Eds.; Springer: Berlin, 2006; Vol. 5, pp 371–402.
289. Knoch, J.; Bjork, M. T.; Riel, H.; Schmid, H.; Riess, W. One-Dimensional Nanoelectronic Devices—Towards the Quantum Capacitance Limit. In *Device Research Conference*; 2008, p 173–176.
290. Knoch, J.; Riess, W.; Appenzeller, J. Outperforming the Conventional Scaling Rules in the Quantum-Capacitance Limit. *IEEE Electron Device Lett.* **2008**, *29*, 372–374.
291. Luisier, M.; Lundstrom, M.; Antoniadis, D. A.; Bokor, J. Ultimate Device Scaling: Intrinsic Performance Comparisons of Carbon-Based, InGaAs, and Si Field-Effect Transistors for 5 nm Gate Length. In *2011 IEEE Int. Electron Devices Meeting (IEDM)* **2011**, p- 11.12.11–11.12.14.
292. Kaasbjerg, K.; Thygesen, K. S.; Jacobsen, K. W. Phonon-Limited Mobility in n-Type Single-Layer MoS_2 from First Principles. *Phys. Rev. B* **2012**, *85*, 115317.
293. Qiu, H.; Pan, L. J.; Yao, Z. N.; Li, J. J.; Shi, Y.; Wang, X. R. Electrical Characterization of Back-Gated Bi-layer MoS_2 Field-Effect Transistors and the Effect of Ambient on Their Performances. *Appl. Phys. Lett.* **2012**, *100*, 123104.
294. Kim, S.; Konar, A.; Hwang, W. S.; Lee, J. H.; Lee, J.; Yang, J.; Jung, C.; Kim, H.; Yoo, J. B.; Choi, J. Y.; et al. High-Mobility and Low-Power Thin-Film Transistors Based on Multi-layer MoS_2 Crystals. *Nat. Commun.* **2012**, *3*, 1011.
295. Liu, H.; Xu, K.; Zhang, X. J.; Ye, P. D. The Integration of High-K Dielectric on Two-Dimensional Crystals by Atomic Layer Deposition. *Appl. Phys. Lett.* **2012**, *100*, 152115.
296. Pradhan, N. R.; Rhodes, D.; Zhang, Q.; Talapatra, S.; Terrones, M.; Ajayan, P. M.; Balicas, L. Intrinsic Carrier Mobility of Multi-Layered MoS_2 Field-Effect Transistors on SiO_2 . arXiv:1301.2813, **2013**.
297. Wang, L.; Sasaki, T.; Ebina, Y.; Kurashima, K.; Watanabe, M. Fabrication of Controllable Ultrathin Hollow Shells by Layer-by-Layer Assembly of Exfoliated Titania Nanosheets on Polymer Templates. *Chem. Mater.* **2002**, *14*, 4827–4832.
298. Ma, R.; Bando, Y.; Sasaki, T. Directly Rolling Nanosheets into Nanotubes. *J. Phys. Chem. B* **2004**, *108*, 2115–2119.
299. Miyamoto, N.; Kuroda, K. Preparation of Porous Solids Composed of Layered Niobate Walls from Colloidal Mixtures of Niobate Nanosheets and Polystyrene Spheres. *J. Colloid Interface Sci.* **2007**, *313*, 369–373.
300. Suzuki, S.; Miyayama, M. Lithium Intercalation Properties of Octatitanate Synthesized through Exfoliation/Reassembly. *J. Phys. Chem. B* **2006**, *110*, 4731–4734.
301. Fukuda, K.; Saida, T.; Sato, J.; Yonezawa, M.; Takasu, Y.; Sugimoto, W. Synthesis of Nanosheet Crystallites of Ruthenate with an A-NaFeO₂-Related Structure and Its Electrochemical Supercapacitor Property. *Inorg. Chem.* **2010**, *49*, 4391–4393.
302. Yui, T.; Kobayashi, Y.; Yamada, Y.; Tsuchino, T.; Yano, K.; Kajino, T.; Fukushima, Y.; Torimoto, T.; Inoue, H.; Takagi, K. Photochemical Electron Transfer through the Interface of Hybrid Films of Titania Nano-sheets and Mono-dispersed Spherical Mesoporous Silica Particles. *Phys. Chem. Chem. Phys.* **2006**, *8*, 4585–4590.
303. Miyamoto, N.; Yamada, Y.; Koizumi, S.; Nakato, T. Extremely Stable Photoinduced Charge Separation in a Colloidal System Composed of Semiconducting Niobate and Clay Nanosheets. *Angew. Chem., Int. Ed.* **2007**, *46*, 4123–4127.
304. Sato, H.; Okamoto, K.; Tamura, K.; Yamada, H.; Saruwatari, K.; Kogure, T.; Yamagishi, A. A Heterojunction Photodiode Operating at Inorganic Nanosheet Interfaces. *Appl. Phys. Express* **2008**, *1*, 35001.
305. Rabu, P.; Drillon, M. Layered Organic–Inorganic Materials: A Way towards Controllable Magnetism. *Adv. Eng. Mater.* **2003**, *5*, 189–210.
306. Liu, Z.; Ma, R.; Osada, M.; Iyi, N.; Ebina, Y.; Takada, K.; Sasaki, T. Synthesis, Anion Exchange, and Delamination of Co–Al Layered Double Hydroxide: Assembly of the Exfoliated Nanosheet/Polyanion Composite Films and Magneto-Optical Studies. *J. Am. Chem. Soc.* **2006**, *128*, 4872–4880.
307. Osada, M.; Itose, M.; Ebina, Y.; Ono, K.; Ueda, S.; Kobayashi, K.; Sasaki, T. Gigantic Magneto-Optical Effects Induced by (Fe/Co)-Cosubstitution in Titania Nanosheets. *Appl. Phys. Lett.* **2008**, *92*, 253110.
308. Suzuki, S.; Miyayama, M. Lithium Intercalation Properties of Reassembled Titanate/Carbon Composites. *J. Electrochem. Soc.* **2007**, *154*, A438–A443.
309. Osada, M.; Ebina, Y.; Takada, K.; Sasaki, T. Gigantic Magneto-Optical Effects in Multilayer Assemblies of Two-Dimensional Titania Nanosheets. *Adv. Mater.* **2006**, *18*, 295.
310. Sofos, M.; Goldberger, J.; Stone, D. A.; Allen, J. E.; Ma, Q.; Herman, D. J.; Tsai, W.-W.; Lauhon, L. J.; Stupp, S. I. A Synergistic Assembly of Nanoscale Lamellar Photoconductor Hybrids. *Nat. Mater.* **2009**, *8*, 68–75.
311. Hwang, C. S. Thickness-Dependent Dielectric Constants of (Ba,Sr)TiO₃ Thin Films with Pt or Conducting Oxide Electrodes. *J. Appl. Phys.* **2002**, *92*, 432–437.
312. Osada, M.; Ebina, Y.; Funakubo, H.; Yokoyama, S.; Kiguchi, T.; Takada, K.; Sasaki, T. High-K Dielectric Nanofilms Fabricated from Titania Nanosheets. *Adv. Mater.* **2006**, *18*, 1023–1027.
313. Kim, J. Y.; Osterloh, F. E.; Hiramatsu, H.; Dumas, R. K.; Liu, K. Synthesis and Real-Time Magnetic Manipulation of a Biaxial Superparamagnetic Colloid. *J. Phys. Chem. B* **2005**, *109*, 11151–11157.
314. Nakato, T.; Hashimoto, S. Dispersion of Layered Hexanobate in Organic Solvents through Silylation and Liquid Crystalline Behavior of the Colloidal Suspension. *Chem. Lett.* **2007**, *36*, 1240–1241.
315. Miyamoto, N.; Nakato, T. Liquid Crystalline Nanosheet Colloids with Controlled Particle Size Obtained by Exfoliating Single Crystal of Layered Niobate $\text{K}_4\text{Nb}_6\text{O}_{17}$. *J. Phys. Chem. B* **2004**, *108*, 6152–6159.
316. Miyamoto, N.; Yamamoto, S.; Shimasaki, K.; Harada, K.; Yamauchi, Y. Exfoliated Nanosheets of Layered Perovskite $\text{KCa}_2\text{Nb}_3\text{O}_{10}$ as an Inorganic Liquid Crystal. *Chem. Asian J.* **2011**, *6*, 2936–2939.
317. Krivanek, O. L.; Chisholm, M. F.; Nicolosi, V.; Pennycook, T. J.; Corbin, G. J.; Dellby, N.; Murfitt, M. F.; Own, C. S.; Szilagyi, Z. S.; Oxley, M. P.; et al. Atom-by-Atom Structural and Chemical Analysis by Annular Dark-Field Electron Microscopy. *Nature* **2010**, *464*, 571–574.
318. Choi, T.; Ruggiero, C. D.; Gupta, J. A. Tunneling Spectroscopy of Ultrathin Insulating Cu_2N Films, and Single Co Adatoms. *J. Vac. Sci. Technol., B* **2009**, *27*, 887–890.

319. Balandin, A. A.; Ghosh, S.; Bao, W. Z.; Calizo, I.; Teweldebrhan, D.; Miao, F.; Lau, C. N. Superior Thermal Conductivity of Single-Layer Graphene. *Nano Lett.* **2008**, *8*, 902–907.
320. *Thermophysical Properties of Matter*; Touloukian, Y. S., Ed.; IFI/Plenum: New York, 1970.
321. Sichel, E. K.; Miller, R. E.; Abrahams, M. S.; Buiochi, C. J. Heat-Capacity and Thermal-Conductivity of Hexagonal Pyrolytic Boron-Nitride. *Phys. Rev. B* **1976**, *13*, 4607–4611.
322. Hwang, J.; Kim, M.; Campbell, D.; Alsalman, H. A.; Kwak, J. Y.; Shivaraman, S.; Woll, A. R.; Singh, A. K.; Henning, R. G.; Gorantla, S.; Rummeli, M. H.; Spencer, M. J. van der Waals Epitaxial Growth of Graphene Sapphire by CVD without a Metal Catalyst. *ACS Nano* **2013**, *7*, 385–395.
323. Sakurai, M.; Tada, H.; Saiki, K.; Koma, A. Van Der Waals Epitaxial Growth of C_{60} Film on a Cleaved Face of MoS_2 . *Jpn. J. Appl. Phys.* **1991**, *30*, L1892–L1894.
324. Yamada, H.; Ueno, K.; Koma, A. Preparation of GaS Thin Films by Molecular Beam Epitaxy. *Jpn. J. Appl. Phys.* **1996**, *35*, L568–L570.
325. Enomoto, H.; Kawano, T.; Kawaguchi, M.; Takano, Y.; Sekizawa, K. van der Waals Growth of Thin TaS_2 on Layered Substrates by Chemical Vapor Transport Technique. *Jpn. J. Appl. Phys.* **2004**, *43*, L123–L126.
326. Klein, A.; Tiefenbacher, S.; Eyert, V.; Pettenkofer, C.; Jaegermann, W. Electronic Properties of WS_2 Monolayer Films. *Thin Solid Films* **2000**, *380*, 221–223.
327. Klein, A.; Tiefenbacher, S.; Eyert, V.; Pettenkofer, C.; Jaegermann, W. Electronic Band Structure of Single-Crystal and Single-Layer WS_2 : Influence of Interlayer van der Waals Interactions. *Phys. Rev. B* **2001**, *64*, 204416.
328. Kreis, C.; Traving, M.; Adelung, R.; Kipp, L.; Skibowski, M. Tracing the Valence Band Maximum during Epitaxial Growth of HfS_2 on WSe_2 . *Appl. Surf. Sci.* **2000**, *166*, 17–22.
329. Loher, T.; Ueno, K.; Koma, A. van der Waals Type Buffer Layers: Epitaxial Growth of the Large Lattice Mismatch System $CdS/InSe/H-Si(111)$. *Appl. Surf. Sci.* **1998**, *130*, 334–339.
330. Schlaf, R.; Lang, O.; Pettenkofer, C.; Jaegermann, W.; Armstrong, N. R. Experimental Determination of Quantum Dipoles at Semiconductor Heterojunctions Prepared by van der Waals Epitaxy: Linear Correction Term for the Electron Affinity Rule. *J. Vac. Sci. Technol., A* **1997**, *15*, 1365–1370.
331. Schlaf, R.; Lang, O.; Pettenkofer, C.; Jaegermann, W. Band Lineup of Layered Semiconductor Heterointerfaces Prepared by van der Waals Epitaxy: Charge Transfer Correction Term for the Electron Affinity Rule. *J. Appl. Phys.* **1999**, *85*, 2732–2753.
332. Li, H. D.; Wang, Z. Y.; Kan, X.; Guo, X.; He, H. T.; Wang, Z.; Wang, J. N.; Wong, T. L.; Wang, N.; Xie, M. H. The van der Waals Epitaxy of Bi_2Se_3 on the Vicinal $Si(111)$ Surface: An Approach for Preparing High-Quality Thin Films of a Topological Insulator. *New J. Phys.* **2010**, *12*, 103038.
333. Gehring, P.; Gao, B. F.; Burghard, M.; Kern, K. Growth of High-Mobility Bi_2Te_2Se Nanoplatelets on hBN Sheets by van der Waals Epitaxy. *Nano Lett.* **2012**, *12*, 5137–5142.
334. Wisotzki, E.; Klein, A.; Jaegermann, W. Quasi van der Waals Epitaxy of $ZnSe$ on the Layered Chalcogenides $InSe$ and $GaSe$. *Thin Solid Films* **2000**, *380*, 263–265.
335. Ohuchi, F. S.; Shimada, T.; Parkinson, B. A.; Ueno, K.; Koma, A. Growth of $MoSe_2$ Thin-Films with van der Waals Epitaxy. *J. Cryst. Growth* **1991**, *111*, 1033–1037.
336. Jaegermann, W.; Rudolph, R.; Klein, A.; Pettenkofer, C. Perspectives of the Concept of van der Waals Epitaxy: Growth of Lattice Mismatched $GaSe(0001)$ Films on $Si(111)$, $Si(110)$ and $Si(100)$. *Thin Solid Films* **2000**, *380*, 276–281.
337. Fritsche, R.; Wisotzki, E.; Thissen, A.; Islam, A.; Klein, A.; Jaegermann, W.; Rudolph, R.; Tonti, D.; Pettenkofer, C. Preparation of a $Si(111)$: $GaSe$ van der Waals Surface Termination by Selenization of a Monolayer Ga on $Si(111)$. *Surf. Sci.* **2002**, *515*, 296–304.
338. Endo, M.; Sasago, M.; Ueno, A.; Nomura, N. Characterization of Diazonaphthoquinone Novolac Resin-Type Positive Photoresist for G-Line and I-Line Exposure Using Water-Soluble Contrast Materials. *J. Vac. Sci. Technol., B* **1989**, *7*, 565–568.
339. Loher, T.; Tomm, Y.; Klein, A.; Su, D.; Pettenkofer, C.; Jaegermann, W. Highly Oriented Layers of the Three-Dimensional Semiconductor $CdTe$ on the Two-Dimensional Layered Semiconductors $MoTe_2$ and WSe_2 . *J. Appl. Phys.* **1996**, *80*, 5718–5722.
340. Yang, Y. K.; Chen, H. Y.; Li, D. M.; Yuan, D. Q.; Zheng, B.; Yu, S.; Zou, G. T. The Growth of $PbTe$ on H-Terminated $Si(111)$ Substrate by Hot Wall Epitaxy. *Infrared Phys. Technol.* **2003**, *44*, 299–301.